Energy and Technology Review

Lawrence Livermore National Laboratory

October 1988

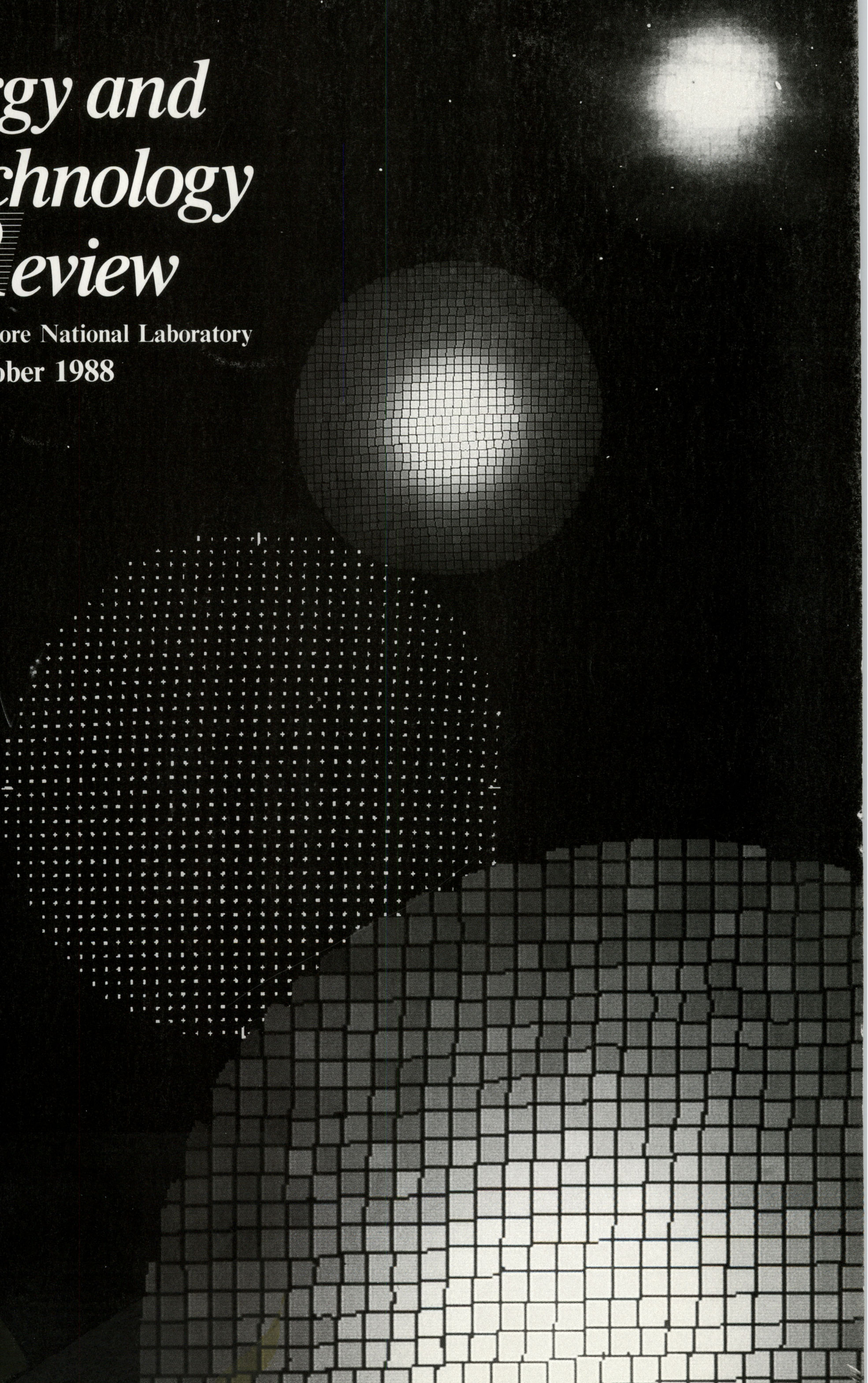

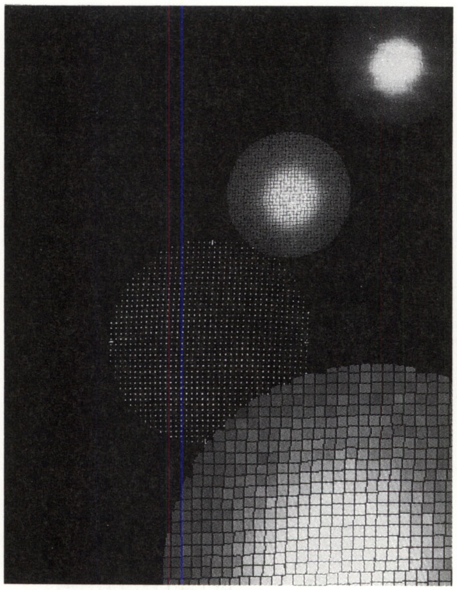

About the Cover

Our cover suggests the many different forms assumed by a coded neutron image as it is recorded and refined for interpretation. The cover images are drawn from our lead article "Neutron Penumbral Imaging," in which we describe our new method of producing coded images of neutrons escaping the deuterium-tritium burn region within an imploding fusion target. This technique, which for the first time allows us to make direct measurements of the burn region, has earned one of *Research and Development* magazine's R&D-100 awards, presented September 22, 1988.

Prepared for **DOE** under contract
No. W-7405-Eng-48

About the Journal

The Lawrence Livermore National Laboratory, operated by the University of California for the United States Department of Energy, was established in 1952 to do research on nuclear weapons and magnetic fusion energy. Since then, we have added other major programs, including laser fusion and laser isotope separation, biomedical and environmental sciences and applied energy technology. Our most recent major program, for the Strategic Defense Initiative Organization, is research on the free-electron laser. These programs, in turn, require research in basic scientific disciplines, including chemistry and materials science, computer science and technology, engineering, and physics. The Laboratory also carries out a variety of projects for other Federal agencies. *Energy and Technology Review* is published monthly to report on unclassified work in all our programs. A companion journal, *Research Monthly*, reports on weapons research and other classified programs. Titles of recent articles published in *Energy and Technology Review* are listed at the back of the journal. Please address any correspondence concerning *Energy and Technology Review* to Mail Stop L-26, Lawrence Livermore National Laboratory, P.O. Box 808, Livermore, CA 94551.

Energy and Technology Review

October 1988

Neutron Penumbral Imaging of Laser-Fusion Targets 1
Using our new penumbral-imaging diagnostic, we have obtained the first images that can be used to measure directly the deuterium-tritium burn region in laser-driven fusion targets.

Computed Tomography for Nondestructive Evaluation 9
Various computed tomography systems and computational techniques are used in nondestructive evaluation.

Three-Dimensional Image Analysis for Studying Nuclear Chromatin Structure 23
We have developed an optic-electronic system for acquiring cross-sectional views of cell nuclei, and computer codes to analyze these images and reconstruct the three-dimensional structures they represent.

Imaging in the Nuclear Test Program 30
Advanced techniques produce images of unprecedented detail and resolution from Nevada Test Site data.

Computational X-Ray Holography 37
Visible-light experiments and numerically simulated holograms test our ideas about an x-ray microscope for biological research.

Abstracts 44

Scientific Editor
Andrew J. Poggio

Editorial Staff
Richard Crawford
Lauren de Vore
Kevin Gleason
Derek P. Hendry
Robert Kirvel
Nona M. Sanford
Shirley O. Taft

Art Staff
Lynn M. Costa
Paul M. Harding
George Kitrinos
Raymond Marazzi
John Zych

Compositor
Louisa Cardoza

Printed in the United States of America
Available from
National Technical Information Service
U.S. Department of Commerce
5285 Port Royal Road
Springfield, Virginia 22161
Price codes: printed copy A02, microfiche A01

UCRL-52000-88-10
Distribution Category UC-700
October 1988

Neutron Penumbral Imaging of Laser-Fusion Targets

Using a new technique, penumbral coded-aperture imaging, we have obtained the first neutron images of laser-driven, inertial confinement fusion targets. With these images we can measure directly the deuterium-tritium burn region within a compressed target.

For further information contact
Richard A. Lerche (415) 422-5364
or David B. Ress (415) 423-8195.

A long-term goal of LLNL's Inertial Confinement Fusion Program is to demonstrate that electric power can be produced by imploding targets containing deuterium-tritium (D-T) fuel. Our expectation is that such power can be made commercially competitive with power from other sources.

Efficient energy production requires that inertial confinement fusion (ICF) targets produce about 100 times more energy than is used to drive the implosion. Such high gain can be achieved by using laser energy to compress the fuel. Most of the fuel is compressed to a density of a few hundred grams per cubic centimeter at a relatively low ion temperature (~1 keV). At the center of the highly compressed fuel is a small "hot spot" containing about 1% of the fuel mass at a much lower density (on the order of 30 g/cm^3) but higher ion temperature (~4 keV). Fusion starts in this central hot spot with the release of energetic neutrons and alpha particles. The reaction advances into the surrounding, highly compressed fuel via a spherical, thermonuclear burn wave that propagates by energy transfer from the alpha particles to the D-T plasma.

We use images of the burning fuel to verify calculations of the implosion physics and to determine the existence of asymmetries. However, viewing a target with sufficient resolution is extremely difficult, and previous methods have not been completely satisfactory. For example, x-ray emission, which is the basis for many widely used ICF diagnostic instruments, depends on the spatial and temporal profiles of plasma density, ionization state, and electron temperature. During an ICF implosion, ion and electron temperatures can be quite different, and mixing of target components leads to complicated spatial variations in the ionization state. Thus, an x-ray image provides information about the spatial structure of several complex processes within the target that are not directly related to hot-spot formation, fuel ignition, or the fusion reaction.

A neutron image, on the other hand, provides a direct measurement of the spatial extent of fusion reactions. Furthermore, in targets that achieve high compression, most reaction products and x rays are absorbed within the target while the penetrating neutrons escape unperturbed. It is for this reason that neutron imaging has long been recognized for its potential to diagnose unambiguously both compression and hot-spot formation in burning fuel.[1]

Many of our future ICF experiments with our Nova laser will focus on the physics of hot-spot formation, and we will require measurement techniques such as neutron imaging. Relevant implosions will produce neutron emission from regions 20 μm in diameter with yields of 10^{11} neutrons per implosion. Conventional pinhole imaging is not sensitive enough to produce neutron images of such targets; even with a larger neutron yield, the techniques for fabricating the required pinhole are not yet developed. Penumbral imaging, a technique recently developed to obtain x-ray images of laser-produced plasmas,[2] is a much more efficient method of imaging neutrons emitted by ICF targets.

Our recent numerical and theoretical calculations verified the feasibility of neutron penumbral imaging. We have now built a system specifically designed to demonstrate the technique of neutron penumbral imaging, and we have obtained excellent experimental results with our preliminary system.[3]

Penumbral Imaging

Penumbral imaging is a two-step technique involving coded-aperture imaging. Coded-image formation (Figure 1) is similar to pinhole imaging but with the essential difference that the aperture is larger than the size of the source. In the first step, a source of incoherent radiation casts a geometrical shadow through a circular aperture, thereby producing a coded image that consists of a bright, uniformly illuminated central region surrounded by a partially illuminated penumbra. All of the information about the spatial distribution of a source is encoded in the penumbra.

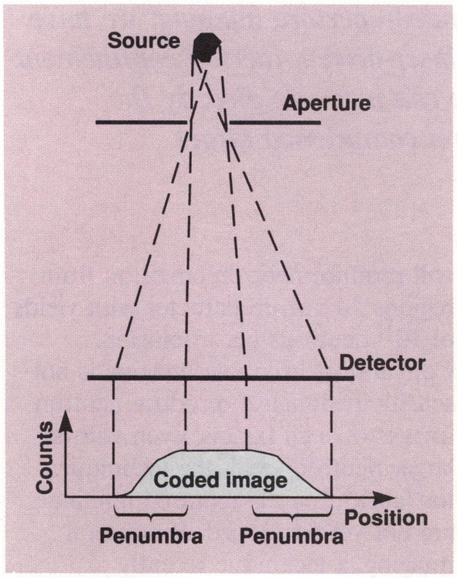

Figure 1. Concept of penumbral imaging. A source casts a geometrical shadow through a circular aperture to produce a coded image. The penumbra of the coded image contains information about the shape of the source. The scale of this figure differs from that for our experimental system, but the principle of operation is the same.

However, because the coded image is the convolution of the source distribution with the aperture transmission function, it does not represent the actual appearance of the source itself. In the second step, the source distribution is deconvolved (i.e., extracted by mathematical techniques) from the coded image. In other words, we decode the image to determine the shape of the original source using numerical techniques and knowledge of the aperture shape.

Aperture Design

To obtain an image of the highly penetrating, 14-MeV D-T fusion neutrons with the technique of penumbral imaging, the aperture must be thick enough to provide sufficient image contrast; it should also be specially tapered to provide a sharp point-spread function that is invariant with the position of a source (that is, isoplanatic). To provide the necessary contrast, we fabricated our aperture from a gold cylinder. Many of the neutrons are not stopped by the gold but instead are scattered with a mean free path of 3.2 cm. Because our aperture is located quite far from the detector, virtually none of the scattered neutrons is detected.

A particularly satisfactory taper for our aperture is a toroidal segment (Figure 2a) with a radius of curvature *R* (minor radius of the toroid) much greater than the aperture thickness *t*. The principle of the toroidal taper is that rays drawn from various positions in a source plane produce similar cutoffs as they are moved from the edge of the aperture into the torus. Some distortion is introduced because magnification depends on the position of the source point. Our aperture can be regarded as formed from a segment of a toroidal solid; by proper choice of the segment, we can minimize distortion.

Figure 2. (a) Principle of the toroidal segment aperture. To obtain an image of penetrating radiation, the aperture must be thick enough to provide sufficient image contrast and be specially tapered to provide an isoplanatic point-spread function. A particularly satisfactory taper is a toroid with a radius of curvature much greater than the aperture thickness. A practical realization of this concept uses a segment of the toroid. (b) Aperture used in our neutron imaging experiments.

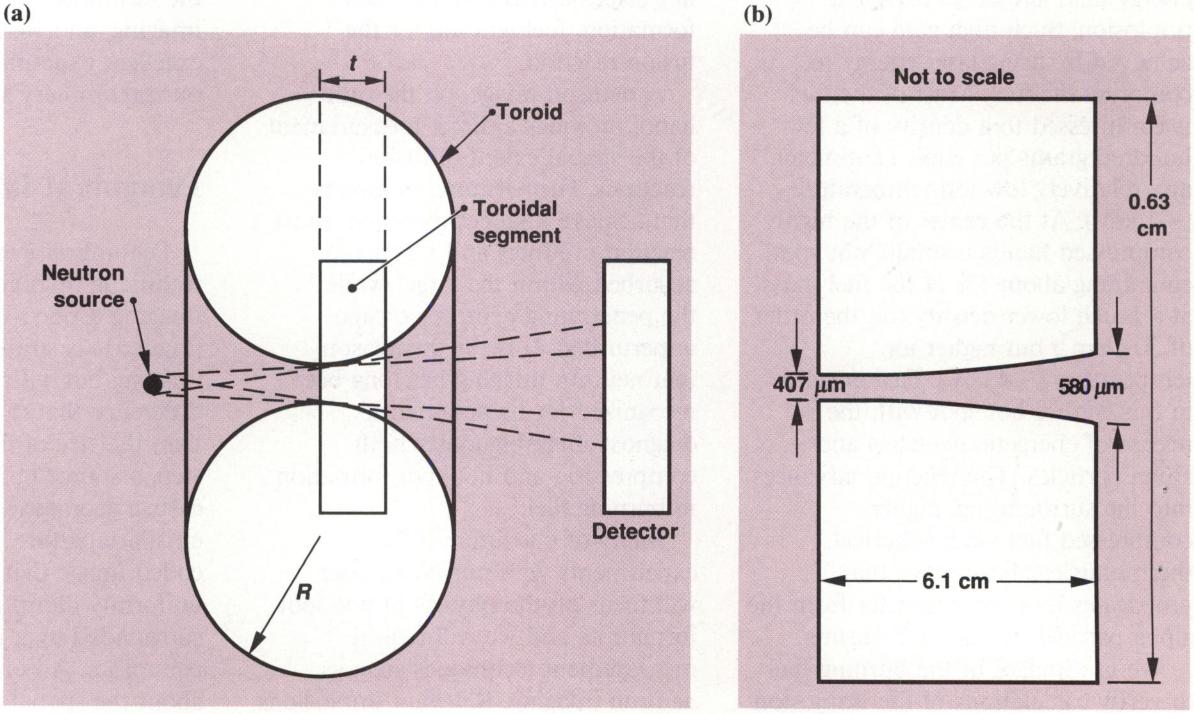

Aperture design is a process of compromise because the optimum dimensions depend on maximum size of the source, source-to-aperture distance, aperture material, and required resolution. The larger the aperture radius of curvature, the sharper the cutoff but the less isoplanatic the response.

We obtained the images that are presented subsequently in this article with the aperture shown in Figure 2b. We made this aperture along the axis of a gold cylinder 0.63 cm in diameter and 6.1 cm long, with a minimum diameter of 407 μm and a radius of curvature of 19.5 m. For this design, the magnification varies by ±3% across the field of view of 400 μm, while the 10%-to-90% width of the cutoff is 30 μm referred to the source plane.

Fabrication of our aperture was greatly simplified, compared to the process required for constructing a pinhole aperture, because the diameter of the opening was large compared to the desired resolution. We fabricated our aperture using an electroforming technique in which gold is electroplated onto a precisely formed brass mandrel. The brass core is then etched out of the gold cylinder to form the aperture itself. Numerical image reconstruction requires precise knowledge of the neutron aperture point-spread function; such information is obtained by careful mechanical characterization of the brass mandrel during fabrication.

Aperture Alignment

Precise alignment of an aperture to the ICF target is critical to our imaging system. The axis of the aperture, which was located 15 cm from the target, had to be pointed to within 50 μm of target center to keep the source within the system's field of view. In addition, the detector, which was located 10.5 m from the target, had to be centered on the axis of the aperture with an accuracy of a few millimeters. We developed a relatively simple technique that allows both rapid and accurate alignment.

Our alignment technique (Figure 3) takes advantage of the properties of coherent light and spherical aberration to form a pair of ring-shaped interference patterns. A slowly converging laser beam illuminates a 2-mm-diameter glass ball positioned at the center of the target chamber. The ball expands the beam and introduces spherical aberration. Plano-convex lenses that are optically centered on each end of the aperture independently cause portions of the beam to slowly converge in a region outside the target chamber. The convex side of the second lens is ground and polished flat over its central region to allow light from the first lens to pass through without effect.

Slowly converging, severely aberrated beams create a long region of interference so that the ring patterns overlap to form a moiré pattern. For our application, the ring patterns were visible over the entire

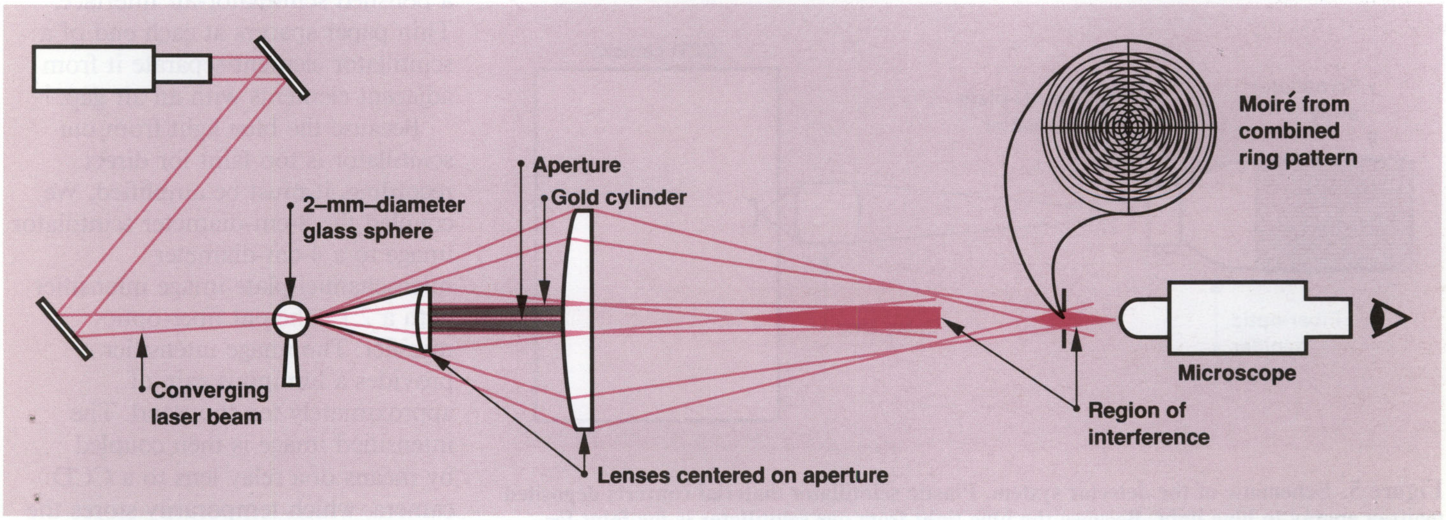

Figure 3. Alignment technique. A 15-mW helium-neon laser located 4.5 m from the 2-mm-diameter glass alignment ball is expanded to a 25-mm diameter and steered with a pair of mirrors. The moiré pattern is viewed through a 50 × microscope attenuated with an optical density of 3.0. The microscope is just outside the target chamber and 2.4 m from the glass sphere. The detector (not shown) is located within the region of interference, 10.5 m from the glass sphere.

10.5-m line of sight of the instrument. Figure 4 shows moiré patterns formed 2.4 m from the target and viewed through the alignment microscope. We mechanically adjust the aperture alignment until the ring patterns are concentric. At this point, the aperture axis is pointed at the center of the alignment ball with the required accuracy. The detector is then centered on the ring pattern to complete the alignment process.

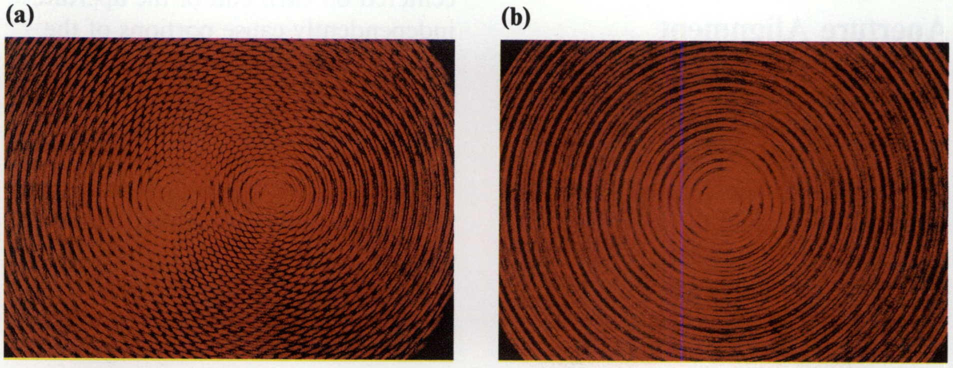

Figure 4. **Moiré patterns formed by the interference of two ring patterns viewed through the alignment microscope. (a) Aperture axis pointing error at the target equal to 126 μm. (b) Aperture axis correctly aligned to the center of the alignment sphere.**

Detector System

The number of neutrons available to form a coded image is relatively small for the targets that are of interest to us. Thus, a primary consideration for choosing a detector system for our imaging experiments was its efficiency for detecting 14-MeV neutrons. The detector system shown in Figure 5 consists of four principal components: a scintillator array, a fiber-optic minifier, an image intensifier, and a charge-coupled-device (CCD) camera.

The heart of the detector system is an 8-cm-diameter circular array of 1240 plastic elements. Each element is a 10-cm-long rod with a square cross section 2 mm on a side. The plastic scintillator material converts the deposited neutron energy to blue light. Within the scintillator, neutrons interact primarily through elastic scattering events with hydrogen nuclei to produce recoil protons that excite the scintillator as they slow down. The cross section of each detector element is matched to the 0.7-mm maximum transverse range of these recoil protons. On average, about 25% of the incident neutron energy is deposited in each element, and blue light is produced in proportion to the amount of energy deposited.

In addition to detecting neutrons, each scintillator element acts as a light guide to transport scintillator light to the output surface of the array. The 10-cm-long sides of each scintillator achieve total internal reflection via a polished scintillator-air interface. Thin paper spacers at each end of a scintillator element separate it from adjacent elements with an air gap.

Because the blue light from our scintillator is too faint for direct recording, it must be amplified. We coupled the 8-cm-diameter scintillator image to a 4-cm-diameter microchannel-plate image intensifier with a 2:1 coherent fiber-optic minifier. The image intensifier provides a luminous gain of approximately ten thousand. The intensified image is then coupled by means of a relay lens to a CCD camera, which temporarily stores the image and converts it to digital form. Digital information is transferred to magnetic storage media with an LSI-11 computer. Figure 6 shows a coded image recorded in this fashion.

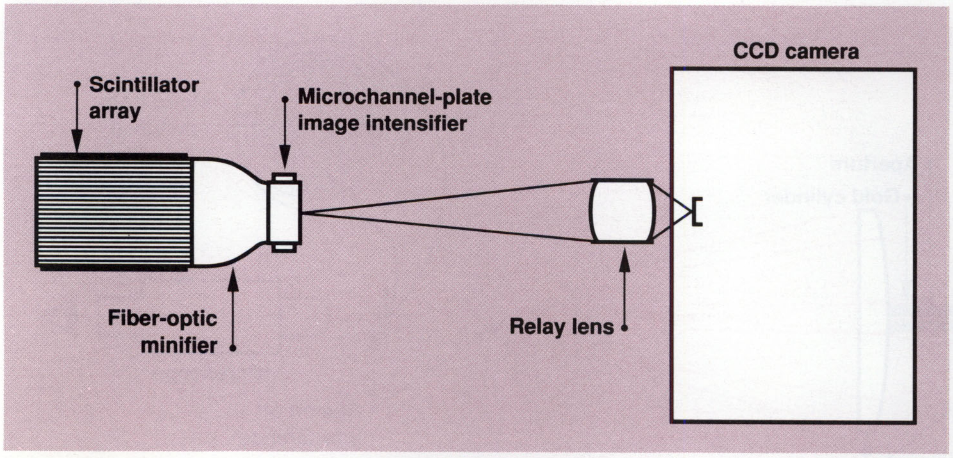

Figure 5. **Schematic of the detector system. Plastic scintillator material converts deposited neutron energy to blue light. Because the blue light from our scintillator is too faint for direct recording, it must be amplified. The 8-cm-diameter scintillator image is coupled to a 4-cm-diameter microchannel-plate image intensifier with a 2:1 fiber-optic minifier. The image intensifier provides a luminous gain of approximately ten thousand. The intensified image is then coupled by means of a relay lens (0.22 × magnification) to a CCD camera, which temporarily stores the image and converts it to digital form.**

Image Reconstruction

As described previously, our recorded image is coded and does not represent the actual appearance of the original source. To obtain a useful image of the source, we must remove from the coded image the distortion caused by our imaging system and deconvolve the effect of the aperture point-spread function.

Characteristics of the imaging system that distort the recorded image include:

- CCD camera offset and fixed-pattern background noise.
- Random dots (salt-and-pepper noise) caused by neutrons traveling through the plastic scintillator and interacting directly in the CCD.
- Uniform background outside the image area caused by neutrons passing directly through the gold that forms the aperture.
- CCD-to-scintillator pixel mapping. (The image is recorded with a 384 × 576-element CCD array; however, the fundamental resolution in a recorded image is limited by each of the 1240 scintillator elements. Thus, we must map each CCD element to its corresponding scintillator element.)
- Spatial variations in detector sensitivity.
- Geometrical distortion introduced by the fiber-optic minifier.
- Nonuniform spacing of scintillator elements.

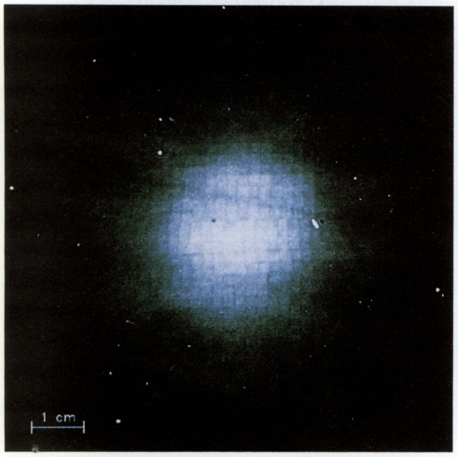

Figure 6. Neutron coded image before reconstruction. Distortions caused by the imaging system that are observable in this image include neutron spikes, uniform background, spatial variation in detector intensity, and nonuniform scintillator-element spacing. This image was recorded for a high-yield target that produced 1.2 × 10^{13} neutrons.

We must remove such instrumental effects from a recorded image before deconvolving the effect of the aperture point-spread function. First, we subtract the fixed-pattern background by using an image recorded during a background test when no neutrons are present. For our images, the number of noise spikes is low relative to the total number of CCD pixels. Each spike extends over only a few pixels, which are easily identified by their large signal relative to the surrounding area.

Because approximately 80 CCD elements record light from each scintillator element, we must generate a one-time CCD-to-scintillator pixel map. We create the map by removing the light-tight front cover of the detector and illuminating the front of the scintillator array with light from a distant source. In the resulting image, CCD elements that lie along scintillator element boundaries have a 5% dip in signal because light is blocked by the paper spacers. We find the signal for each scintillator element by summing the signals recorded in the corresponding CCD elements.

We measure the spatial sensitivity of the detector by exposing the detector to a temporally short, spatially uniform burst of neutrons. We use high-yield shots generating 10^{13} neutrons at Nova with the detector placed 2.5 m from the target and with no aperture in place. From the resulting image, we determine the relative sensitivity for each scintillator element. Each coded image is corrected (or "flat-fielded") for this sensitivity variation. Figure 7 shows the image in Figure 6 after spike removal, CCD-to-scintillator pixel mapping, and flat-fielding.

The fiber-optic minifier introduces noticable geometrical distortion into the image. Figure 8 shows the image

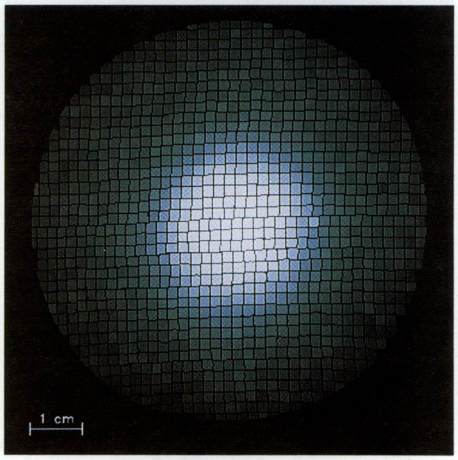

Figure 7. Partially corrected coded image. Shown here is the image in Figure 6 after neutron spike removal, CCD-to-scintillator mapping, and correction.

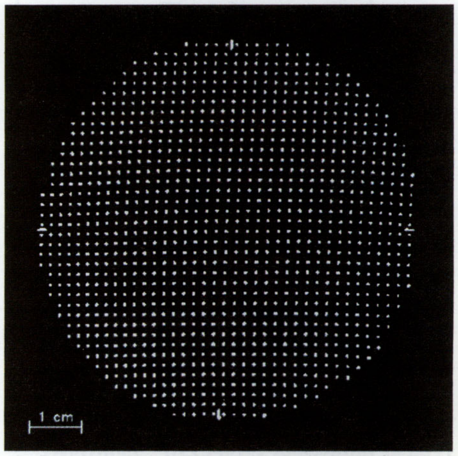

Figure 8. Enhanced image of grid pattern. We used this image of a mask with pinholes located 2 mm apart on a uniformly spaced grid to quantify geometrical distortion in the detector system.

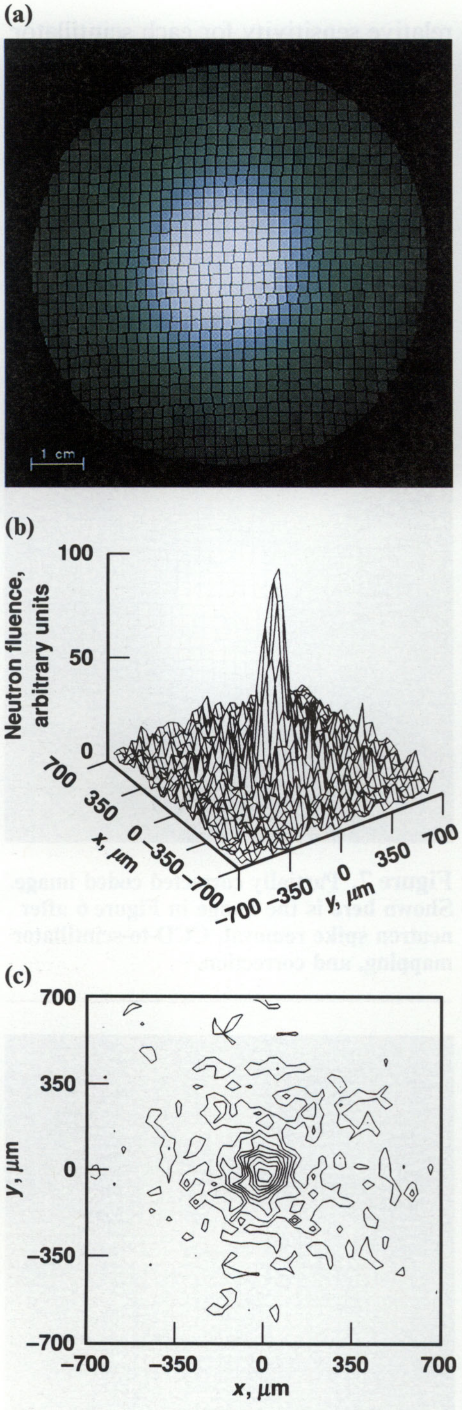

Figure 9. Neutron image recorded for a typical high-yield target (10^{13} neutrons). (a) Coded image. (b) Isometric representation of the reconstructed neutron source. (c) Contour plot of (b) looking downward on the *x-y* plane.

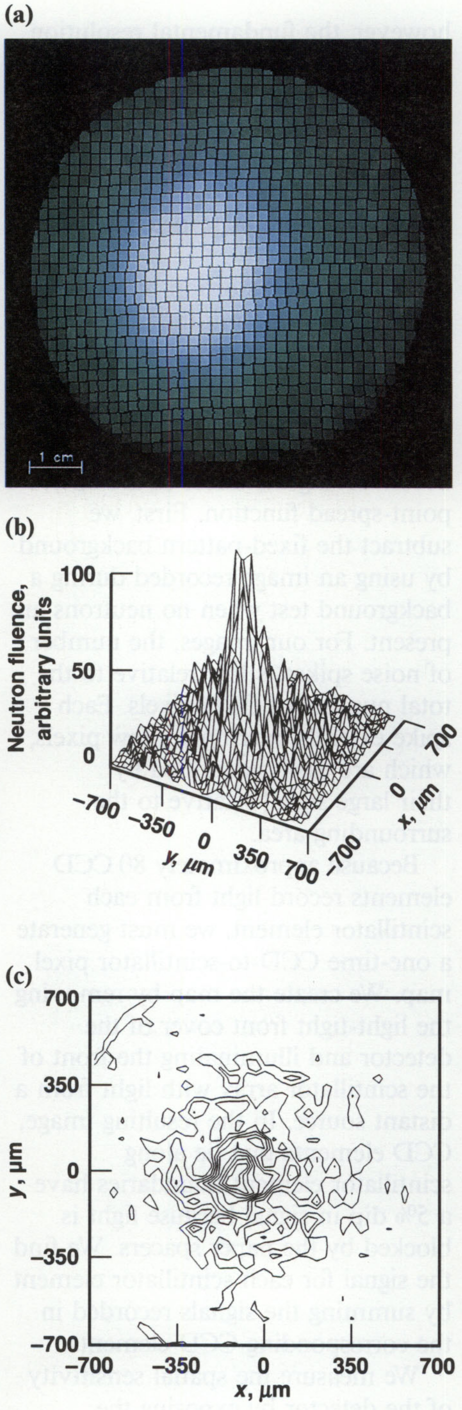

Figure 10. Neutron image recorded for a high-yield target (3 × 10^{12} neutrons) intentionally heated with nonuniform laser light. (a) Coded image. (b) Isometric representation of the reconstructed neutron source. (c) Contour plot of (b) looking downward on the *x-y* plane.

of a mask with pinholes located 2 mm apart on a uniformly spaced grid. The mask is placed in contact with the minifier and illuminated. We use bilinear interpolation to determine the true position of each scintillator element relative to the CCD pixels.

Our deconvolution technique requires the coded image to be comprised of an array of values at uniformly spaced coordinates. Because the scintillator array has nonuniform spacing, we use an additional interpolation step to convert the irregularly spaced data to regularly spaced data.

Recall that our recorded coded image is the convolution of the neutron source distribution and the aperture point-spread function. The effect of the aperture on the coded image must be deconvolved to obtain a neutron source distribution. In penumbral imaging, the Fourier transform of the point-spread function has a central lobe that is much narrower than that of the source, and the side lobes are separated by zeros that extend to higher frequencies. Spatial frequency components that lie close to these zeros have a poor signal-to-noise ratio and must be deemphasized during the deconvolution process. We use a parametric Wiener filter for this purpose. The Wiener filter does not cause distortion of the image but does introduce some low-pass filtering (or blurring). For neutron images from Nova, the loss of resolution is quite small, approximately 15%.

Neutron Images

The neutron images we recorded during recent experiments at Nova illustrate the capabilities of our new imaging diagnostic. The ICF targets were spherical glass shells 1 mm in diameter with walls 2 μm thick; these were filled with 2.5 MPa (25 atm) of equimolar D-T gas. To achieve an implosion, a target is irradiated directly with the Nova laser. The laser consists of two five-beam clusters that produce a complex, asymmetric illumination pattern on the target. More than 20 kJ of 351-nm light is focused onto the target in a 1-ns temporally square pulse. Unlike the optimal target designs discussed previously, these targets do not produce strong fuel compression; instead they generate large neutron yields by achieving a high ion temperature (9 keV). Radial convergence of the glass shell is less than three, thus producing a relatively large neutron-source region compatible with the resolution of our imaging system. Neutron yields varied from 2.0×10^{12} to 1.2×10^{13}, and the duration of the fusion burn was measured with photoconductive devices to be in the range 300–400 ps full width at half maximum (FWHM).[4]

We have obtained images for our high-yield, directly illuminated targets that produce a typical yield of 10^{13} neutrons. Figure 9a is a representative coded neutron image with approximately 15 000 neutrons interacting in each scintillator element within the central bright region. Figures 9b and 9c show reconstructed images of the source, where the pixel size is 35 μm, and the two-point resolution is about 80 μm. The neutron burn region is nearly symmetrical, with an average FWHM of 150 μm. We estimate the signal-to-noise ratio for the peak signal level to be better than 10.

In another type of experiment, we attempted to manipulate the shape of the neutron source region by altering the uniformity of laser illumination. This time, we aimed the beams to preferentially heat opposite sides of the target and to produce an extremely nonuniform drive. The reduced yield was 3.0×10^{12} neutrons. The resulting neutron image is larger and has a more complicated shape (see Figure 10). At the 70% contour, the image is elliptical with the major axis oriented vertically, as expected; at lower contour levels, the image has several distinct lobes.

A detailed hydrodynamic computer code provides theoretical modeling of laser-fusion implosions. The computer calculations, which were carried out in one dimension and thus assume exact spherical symmetry, give neutron yields that are three to four times larger than we experimentally measure. Neutron imaging shows another discrepancy: the simulated neutron image FWHM is smaller by a factor of 15 than the experimental image (Figure 11a). The sharp peaking of the simulated neutron image is

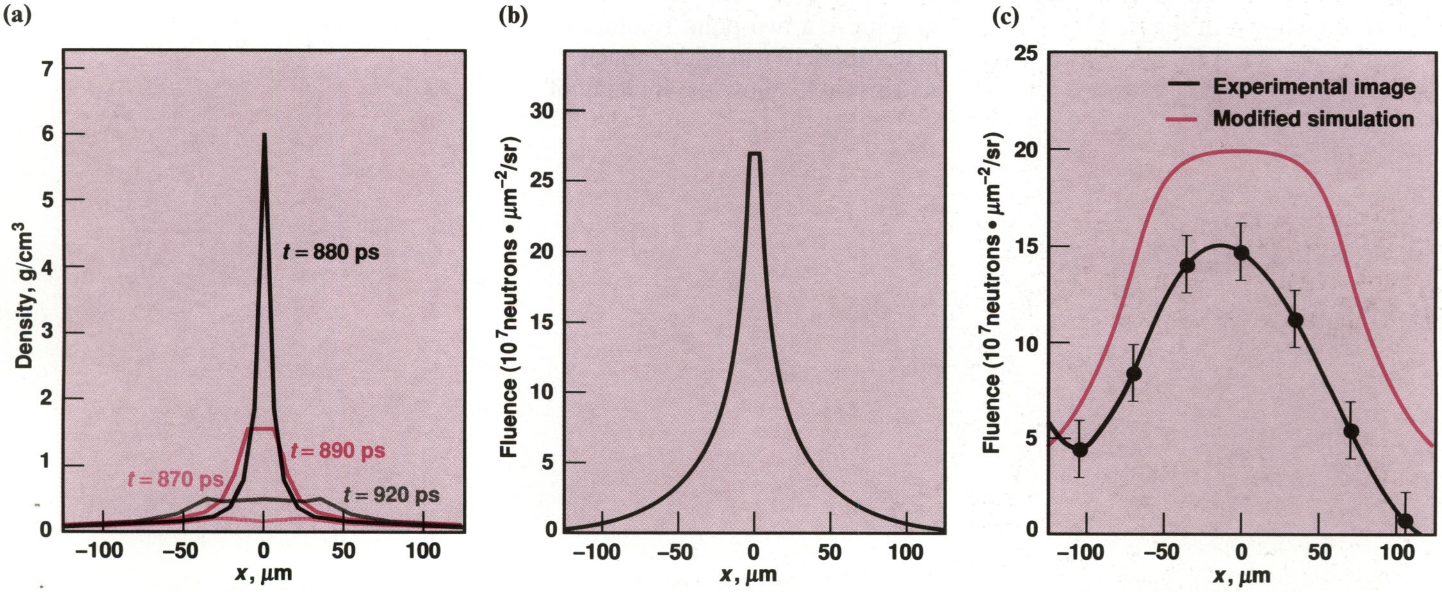

Figure 11. Comparison of measured neutron image with the results of a hydrodynamic computer simulation. (a) Overlay of calculated density profiles at four different times during target implosion showing the strong peaking and, thus, expected high neutron emission rate at the beginning of the D-T burn. (b) Simulated neutron image. (c) The *x*-axis lineout of the experimental image and a simulated neutron image, modified by ignoring the first 50 ps of neutron emission. By deleting the period of strong peaking of density, the calculated image now more closely agrees with our measurements.

caused by a brief, large rise in density at the center of the target (Figure 11b). This strong compression occurs during the first 50 ps of neutron emission and is associated with the final convergence of a spherical shock wave produced by the simulated laser drive. In an actual experiment, however, the laser illumination is asymmetric and may launch a strongly distorted shock front that does not converge neatly at target center, producing a lower-density compressed region that is spatially and temporally broader than the one-dimensional code prediction. This hypothesis is also supported by the neutron-emission-time measurements, which show emission time to be a factor of two to three larger than the simulation results.

Thus, two-dimensional effects appear to reduce the strong emission from the center of the target. We have illustrated this effect by producing a simulated neutron image that ignores the first 50 ps of neutron emission. The result, shown in Figure 11c, is a good match to the experiment. Moreover, the neutron yield corresponding to this portion of the burn is roughly the same as that produced by the experiment. A two-dimensional calculation is required to more accurately model our experiments.

Summary

Information from our preliminary neutron penumbral imaging diagnostic is already providing insight into the physics of laser-fusion implosions. Our recent experiments have demonstrated the new diagnostic tool, neutron penumbral imaging. The performance of our imaging system is in good agreement with predictions based on both numerical and theoretical models. We are now improving the imaging system resolution and sensitivity through changes in the aperture and detector. During future work, we will attempt to achieve a two-point resolution better than 10 μm with enough sensitivity to allow the imaging of radiation-driven targets that achieve high radial convergence and produce neutron yields of 10^{11} or less. Such an enhanced imaging system is certain to become a valuable asset for future ICF research.

Key Words: fusion fuel—deuterium-tritium (D-T); imaging diagnostic—neutron; inertial confinement fusion (ICF); laser—Nova; neutron penumbral imaging.

Notes and References

1. D. T. Attwood et al., *Laser Interaction and Related Plasma Phenomena*, H. J. Schwarz et al., Eds. (Plenum Press, New York, 1981), Vol. 5, pp. 423–463.
2. K. A. Nugent and B. Luther-Davies, "Penumbral Imaging of High-Energy X Rays from Laser-Produced Plasmas," *Opt. Commun.* **49**, 393 (1984).
3. D. Ress, R. A. Lerche, R. J. Ellis, S. M. Lane, and K. A. Nugent, "Neutron Imaging of Laser Fusion Targets," *Science*, **241**, 956 (1988).
4. D. R. Kania et al., "High-Speed Detection of Thermonuclear Neutrons with Solid-State Detectors," *IEEE Trans. Nucl. Sci.* **35**, 387 (1988).

Computed Tomography for Nondestructive Evaluation

We are developing new x-ray tomography data-acquisition hardware and computational techniques for image reconstruction, analysis, and display, making possible the nondestructive evaluation of the internal structure of industrial objects.

For further information contact
S. G. Azevedo (415) 422-8538,
H. E. Martz (415) 423-4269, or
J. M. Brase (415) 422-6992.[1]

A number of analogies can be drawn between a routine medical check-up and assembly-line inspection of critical industrial components (see Table 1). Both are used to ensure that the "object" meets specifications, to enhance its reliability, and to assess its overall "health." One possible method for inspecting internal structure is to cut open the object and examine it (e.g., exploratory surgery). However, noninvasive techniques—those that do not, as a result of the inspection method, damage the object's integrity or health—are preferred. Noninvasive methods of inspection in an industrial setting are called nondestructive evaluation (NDE).[2]

The most common NDE methods involve the measurement of electromagnetic (e.g., x-ray, microwave, infrared), particle (e.g., proton, neutron), or acoustic (e.g., ultrasound, sonar) scattering by the object under evaluation. From these measurements, we can reconstruct an image of the object using absorption and scattering models. One such inspection method, known as computed tomography or CT, was first developed in the early 1970s as a tool for medical diagnostic imaging, and its inventors were awarded the Nobel prize in medicine in 1979.[3] (The basic theory of transmission tomography is described in the box on p. 12.) With CT, unlike standard film radiography, we can obtain true three-dimensional density information about the object. Today, CT is a familiar nonsurgical technique that physicians use to obtain high-resolution pictures of internal organs.

The problems for medical diagnosis and NDE are similar, but there are enough differences to warrant new techniques of inspection. For example, industrial objects may vary widely in size and shape, requiring many different configurations of source, object, and sensors. Also, industrial objects typically have more detailed design information available in the

Table 1. Comparison of typical computed tomography parameters for medical diagnosis and industrial inspection.

	Medical	Industrial
Size, shape, and density of the object	Little variation	Wide range
Spatial resolution requirements	Range: 0.3 to 1 mm	Range: μm to cm
Quantitative results	Not available (images only)	Usually needed (with <0.5% error)
Speed requirements:		
(a) Data acquisition	0.03 to 3 s	High-resolution—days Low quality*—seconds
(b) Reconstruction	<10 s	Seconds to hours
Dosage restrictions	Severe (regulated)	Mild
Motion problem	Yes	Rarely
Prior information available:		
(a) 3D structure	No	Yes
(b) Materials	Minimal	Yes
(c) Accurate templates	No	Yes
(d) Measurement noise	Yes	Yes
Number of projections	180 to 6192	2 to 1000
Number of rays per projection	200 to 300	32 to 512
Number of pixels	$\sim 512^2$	32^2 to 1024^2

* Suitable for assembly-line use.

form of mathematical models from computer-aided design packages. This fact is not exploited in medical CT systems but is useful in NDE.

The most common form of CT uses x-ray illumination of a single plane in the object taken at various angles around the object. The block diagram of a first-generation CT scanner (discrete-beam, single-source/single-detector) in Figure 1 shows how this can be done. An x-ray source and a detector, in fixed positions with respect to each other, are placed on opposite sides of the object. The source and detector are moved together in a transverse plane through the object, called the "slice plane" (or the object itself is moved). The transmitted x-ray intensity values are collected for each individual ray position and stored in the computer. One full scan of all rays at a fixed rotation angle of the object relative to the source-detector axis gives a *projection* of the slice plane for that angle. More projections are taken at different angles. The object or the source-detector pair is rotated so that the beam is always directed in the slice plane. The full set of data is processed in the computer to reconstruct the linear attenuation coefficients (which are proportional to density distributions) of the slice plane as a two-dimensional array. This array or cross-section function is treated as an image and is further processed, displayed, and analyzed.

Instead of the single-ray geometry in Figure 1, a more common arrangement for data acquisition employs many detectors that simultaneously collect multiple rays of a fan-beam (one-dimensional) or cone-beam (two-dimensional) x-ray field. Figure 2 shows these various configurations. Such an arrangement improves data-acquisition times but introduces some degrading effects due to off-axis scattering in the object. Medical systems usually use configurations with a fixed ring of detectors (so-called third- and fourth-generation scanners) designed for high speed and low dosage. However, this arrangement is not flexible enough for most NDE imaging.

The overall goal of current CT research efforts (ours and others') is to improve the three types of resolution that characterize tomography scanning systems, namely:

- Spatial resolution—the sizes of detectable objects.
- Contrast resolution—the discernible density differences of subregions in an object.
- Temporal resolution—the speed of data collection and processing.

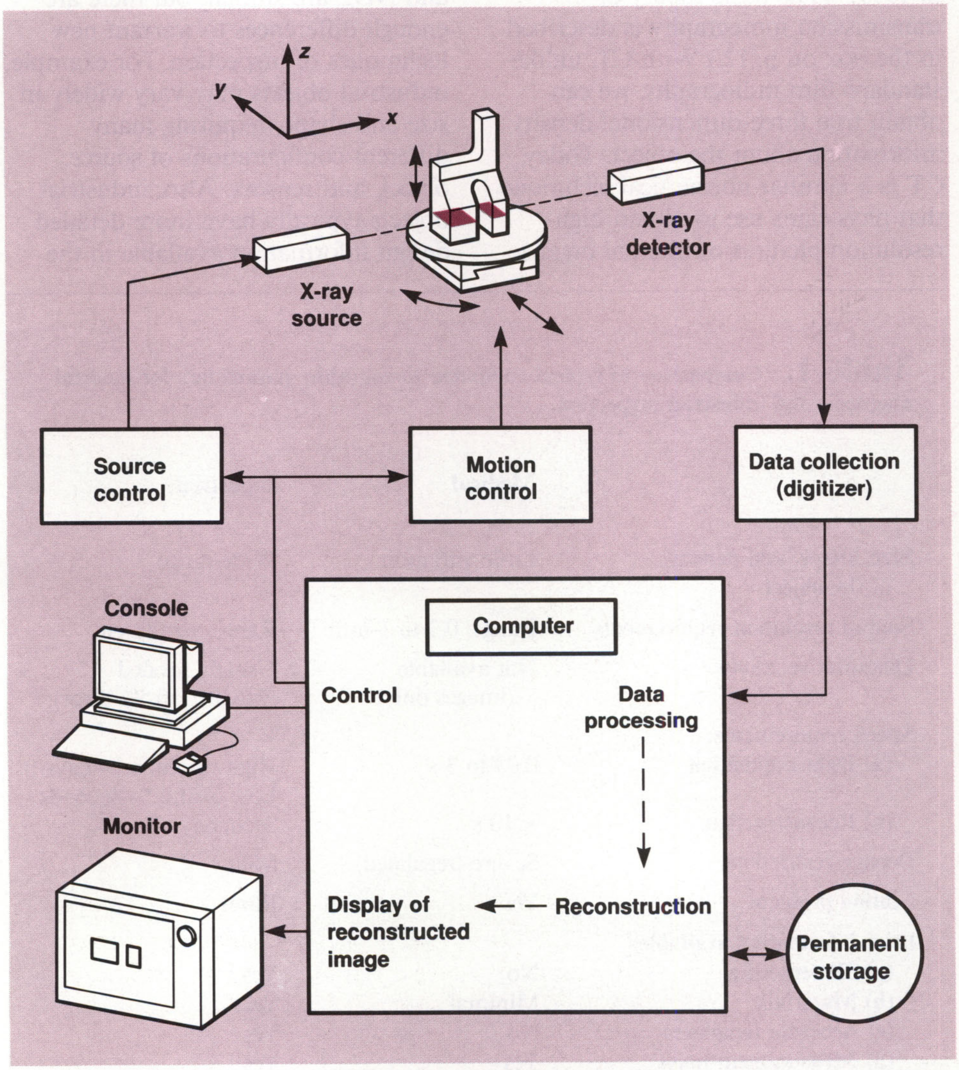

Figure 1. A first-generation, single discrete-beam CT system. The x-ray source and associated detector are located on opposite sides of the target object. The transmitted x-ray intensities are collected and stored for each ray position; a full scan of all rays at a fixed angle gives a projection of the slice plane for that angle.

(a) First generation: single discrete beam

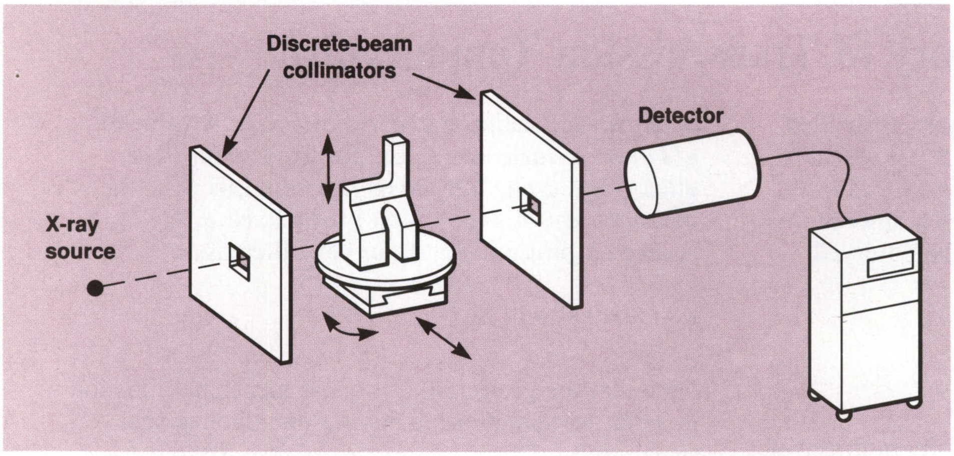

(b) Second generation: fan beam, translate/rotate

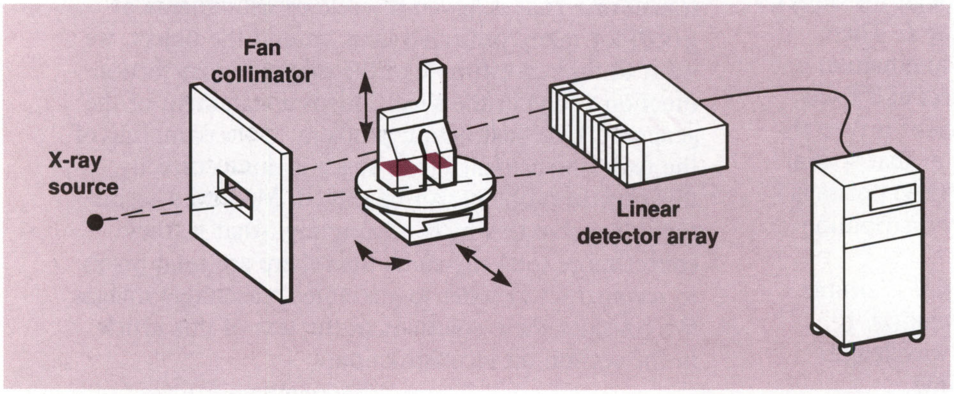

(c) Second generation: cone beam, translate/rotate

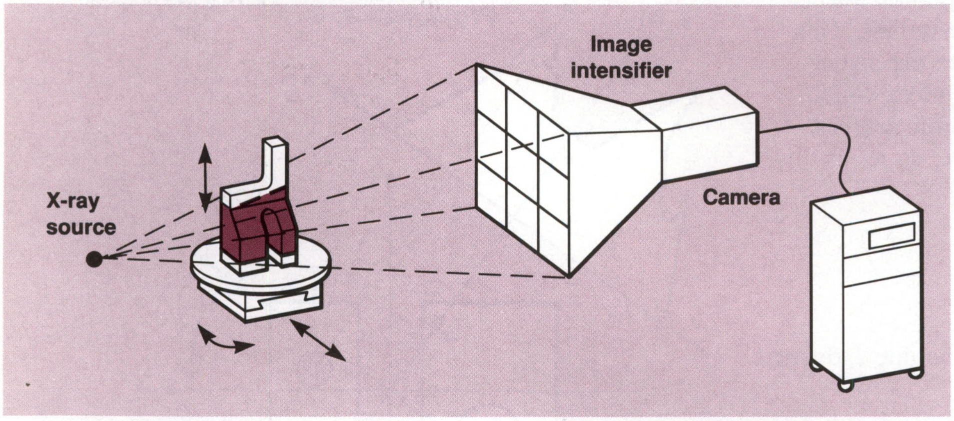

Figure 2. Three CT system configurations used for nondestructive evaluation. (a) The single discrete-beam configuration, similar to that shown in Figure 1. (b) A second-generation fan-beam configuration. (c) A second-generation cone-beam configuration. The fan- and cone-beam configurations use multiple detectors to simultaneously collect multiple rays.

A number of physical issues affect our ability to improve these parameters. These include the randomness in photon counting, finite source and detector apertures, measurement noise, "beam hardening" caused by polychromatic sources, scattering of the beam, limitations of the reconstruction algorithms, and inexact arithmetic used by the computer.

Industrial CT

CT is effectively used in NDE for characterizing materials (for example, measuring local density and uniformity), detecting defects, and verifying assembly. The theory underlying the imaging is the same as in medical CT, except that in many cases our data sets are incomplete or limited. In this section, we explore the implications of limited data.

Reconstructing object cross-sections from projections is a common problem in many scientific and medical areas. The original mathematics for reconstructing a cross-section from its projected line-integrals was developed by Radon in 1917,[4] but his work was overlooked by early researchers in computed tomography.

In a typical NDE problem, we must deal with data sets that are limited or incomplete either due to noise or to our inability to measure certain ray-sums. (See Table 2 for the kinds of limited data and their effects.) Consequently, computed tomography for NDE is still an active area of research.

Situations with missing ray-sums occur because of special circumstances in the object, the geometry, or the

Basic Theory of Transmission Tomography

Parallel-beam transmission tomography is defined on a single plane (fixed z) through an object with a geometry shown in the figure below. As the beam traverses the object, it is attenuated by an amount proportional to the material density. The observed intensity I at the detector is given by

$$I = I_0 \exp\left[- \int_L f(x,y)du \right],$$

where I_0 is the intensity or photon density (number of photons per second per unit cross-sectional area) of the incident beam, L is the beam path through the object, and du is the incremental distance along L. Then $f(x,y)$ denotes the x-ray absorption or attenuation coefficient of the point (x,y) in the object at a fixed vertical plane z. The absorption coefficient is directly proportional to the volumetric density at that spatial position, so a reconstructed image of $f(x,y)$ portrays a two-dimensional nonnegative density distribution within the object.

Note that for a cone-beam geometry, it is simple to extend this model to a third dimension (z). It is also possible to extend it to include wavelength dependence, but for simplicity we assume monochromatic rays here. Wavelength is important, however, since the energy of an x-ray photon affects its degree of attenuation by different materials. This causes so-called beam-hardening, where the higher-energy x rays have a disproportionate effect, which is a very real problem with polychromatic sources.

The measured quantities are I and I_0, so let us define the observed signal on line L as

$$g_L = \ln\left(\frac{I_0}{I}\right) = \int_L f(x,y)du\,.$$

We fill in the explicit equation for the line L defined by s and θ, and write

$$g(s,\theta) = \int_{-\infty}^{\infty} \int_{-\infty}^{\infty} f(x,y)\, \delta(x\cos\theta + y\sin\theta - s)\, dx\, dy\,.$$

The measurement $g(s,\theta)$ has now become a function of two variables, s and θ, and is known as the (two-dimensional) Radon transform of $f(x,y)$. A value of $g(s,\theta)$ on a single line L (i.e., for fixed s and θ) is often called a *line integral* or *ray sum*. Likewise, the measurement of $g(s,\theta)$ at all s for a fixed θ, say θ_0, is called a *projection* and can be written as

$$g_{\theta_0}(s) = g(s,\theta)|_{\theta=\theta_0}\,.$$

Note that the projection is a one-dimensional function in s that we sometimes treat as a one-dimensional signal itself.

We want to find the inverse of the Radon transform. That is, given discrete measurements of $g(s,\theta)$ for many projected lines around the object, we want to find an estimate of the original cross-section function $f(x,y)$ in the slice. This is a statement of the general CT reconstruction problem. If the sampling of the two-dimensional $g(s,\theta)$ space is done correctly, this inverse problem can be solved. Medical systems typically solve this by oversampling—that is, they collect more total ray-sums than there are total pixels to reconstruct in order to guarantee reasonable images. We consider these solutions in the text of this article in the section on reconstruction.

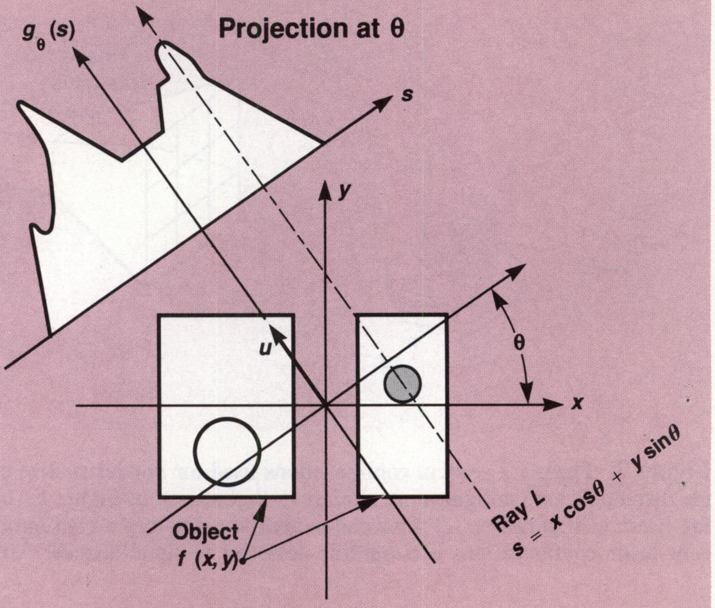

detectors. Of these problems, the most common are opaque objects, large elongated objects, small regions of interest, and tomography in near-real time.

- Opaque objects. The problem of opaque objects is actually one in which the object of interest has mixed densities, or in which some components that we wish to view may be much less dense than others. For example, the object may comprise heavy metals surrounded by foams. This is the hollow-projections problem (see Table 2) and results in streak artifacts radiating from the opaque components.
- Large elongated objects. Large elongated objects cause us problems because we are currently unable to acquire projections of long objects on the full 180-deg arc required. This is the limited-angle problem, which causes anisotropic distortion of the image, especially if flaws are present.
- Small regions of interest. We are often interested in inspecting only a small region of an object at high resolution. One would prefer to minimize the data collection time by intelligently scanning at the few key locations that contain the most information about that small region. This tactic typically leads to truncated projections (part of the object extends beyond the field of view in one or more projections) and gives distorted attenuation values in the region of interest.
- Near-real-time tomography. In practice, time constraints are often important. For example, it is often desirable to obtain a global view of a region (perhaps at low resolution) before embarking on a time-consuming, high-resolution run. Or, for other reasons, we may have only a very few projections from which to reconstruct the image. The image in these cases is underdetermined and typically has various streaking and blurring artifacts.

Besides these four common problems, we must also deal with noise from various sources and with inaccuracies caused by the measurement and computing equipment. As described later, detailed computational models of the inspected object, which are unavailable to medical CT scanners, can help improve the limited-data reconstructions. First, however, let us describe the CT scanning systems currently in use and being developed at the Laboratory.

CT Scanning Systems at LLNL

Because of the problems described above, commercial CT scanners built specifically for NDE have been available only since 1984. These systems have been expensive and not suitable for the broad range of purposes we find at LLNL, which spans the spectrum of object size, shape, and required resolution.

Since we reported the beginning of our CT work (March 1987),[5] we have had to build a number of scanners for Laboratory programs. We now have three operational x-ray CT scanning systems: a video-based cone-beam system (VCAT), a pencil-beam system (PBCAT), and a medium-energy CT system (MECAT). Another system, using illumination by a proton beam, was developed in collaboration with Sandia National Laboratories, Livermore (SNLL). In this system, LLNL provided a proton source from a tandem Van de Graff accelerator and the reconstruction

Table 2. **Types of limited data in computed tomography.**

Limited data	Description	Artifacts
Few projections:		
Limited-angle	$N_\theta < \pi/\Delta_\theta$; good angular sampling over a small range of angles	Anisotropic distortion
Limited-view	$\Delta_\theta > 1/\Omega D$; poor angular sampling over all the object	Blurring
Few rays:		
Spatial aliasing	$\Delta_s > 1/2\Omega$; poor angular sampling	Blurring
Truncated projections	$N_s < D/\Delta_s$; outer rays missing	Streaks
Hollow projections	$N_s < D/\Delta_s$; inner rays missing	Streaks
Inexact arithmetic	Discretization, finite precision, low dynamic range, etc.	High-frequency noise
Measurement noise	Counting statistics, centering error, model mismatch, etc.	All of the above

Legend:
N_θ = Number of projection angles
Δ_θ = Angular distance between projection (radians)
D = Spatial extent (diameter) of the object inspected
Ω = Spatial frequency bandwidth
N_s = Number of detectors or "rays" per projection
Δ_s = Detector spacing

software, and SNLL provided an ion microbeamline and the CT system and electronics.[6] Several other machines are in various stages of design and assembly. All of these systems are assembled in a modular fashion so that improvements in any one component (e.g., better detector technology) can be retrofitted easily.

A plot of CT system performance in terms of spatial resolution versus x-ray energy is shown in Figure 3. (Scanners can be characterized in many ways; this figure provides an illustration of our capabilities.) The devices shown are state-of-the-art machines designed to be responsive to our wide-ranging needs. Below, we describe these systems and briefly list the additional systems we plan to build and use in the next two years.

The Video CAT System

A diagram of the VCAT system is shown in Figure 4. The object to be inspected is illuminated by x rays in a fan beam or cone beam (adjusted by source collimators) from a microfocus tube source (spot size adjustable from 10 to 200 μm). The transmitted rays are detected by one of two possible detector systems. The first is a standard fluoroscopic system using a scintillator for x-ray-to-light conversion, an image intensifier for amplification, and a video camera for "reading" the image. One or more lines of the video signal are extracted and digitized. These data furnish a set of ray sums (see box on p. 12) for the particular projection being imaged. The object is rotated stepwise through one revolution, with data collected at each step. Several video frames can be averaged at each step to improve the signal-to-noise ratio. The microfocus source allows us to use geometric magnification to increase spatial resolution by permitting changes in the relative locations of source, object, and detectors.

The resolution will ultimately be limited both by the finite focal-spot size of the x-ray source ($\sim$10 μm) and the relatively low signal-to-noise ratio of the video system. In addition, nonlinearities in the video system from pixel to pixel and low dynamic range have caused artifacts in the reconstructed images. To solve these problems, we can replace the intensifier system with the second detector system—an unintensified system that uses a thermoelectrically cooled charged-coupled device (CCD) detector system. The CCD has a dynamic range of several orders of magnitude. The VCAT system provides x-ray images in the energy range from 25 to 160 keV, currently limited by the source. The object can be as large as about 0.1 m^3 (limited by the size of the system's cabinet). We have achieved resolutions in the range of 25 μm. Also, because we use a fan- or cone-beam geometry, the data-acquisition times are relatively small compared with the pencil-beam CAT system.

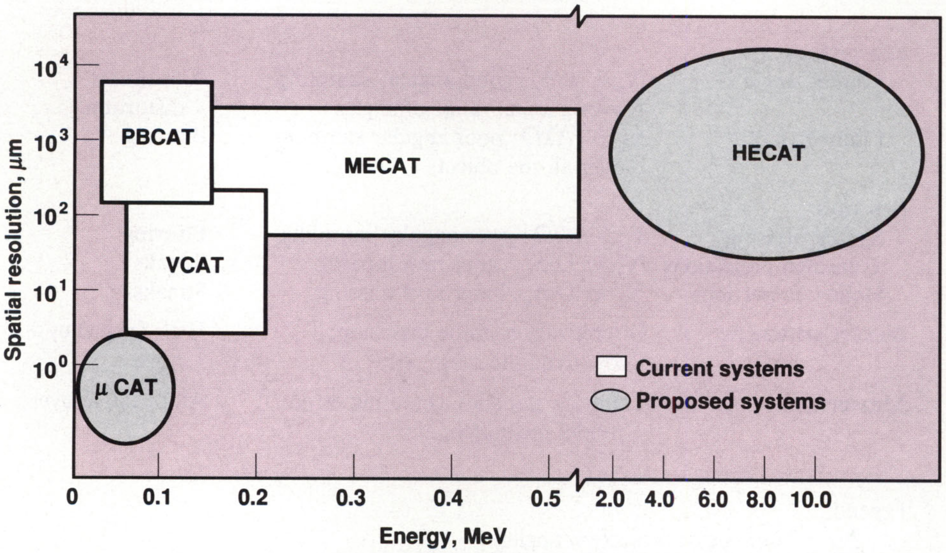

Figure 3. A rough comparison of the LLNL CT system performance in terms of spatial resolution versus x-ray energy. (VCAT: Video-computed axial tomography system. PBCAT: Pencil-beam CAT system. MECAT: Medium-energy CAT system. HECAT: High-energy CAT system. μCAT: High-resolution micro-CAT system.)

The Pencil-Beam CAT System

The pencil-beam CAT (PBCAT) system is shown in Figure 5. The object to be imaged is illuminated with a tightly collimated beam of radiation from radioisotopic sources. We currently use cadmium-109 (22, 25, and 88 keV) and americium-241 (60 keV). We use a high-purity intrinsic germanium detector in conjunction with gamma-ray spectroscopy electronics and a multichannel analyzer. We can record the entire energy spectrum of the radioisotope source or make measurements at specific energies. This type of instrumentation allows us to use a polychromatic x-ray source and simultaneously image several energy regions. We have demonstrated the capability of this system on a prototype unit, and we are in the process of assembling a deliverable PBCAT system.

A disadvantage of PBCAT with isotopic sources is their low specific activity (and resultant low x-ray flux) as compared to x-ray tubes. The smallest practical collimator size with radioisotopes is about 0.25 mm; with this aperture size the counting rate is very low, and it can take days to acquire a single image. We are now in the process of modifying the system so that we can replace the radioisotopes with an x-ray tube. This will improve the spatial resolution and reduce the data-acquisition time.

Currently, the PBCAT system can tolerate x rays in the range from 6 to 125 keV. The object can be as large as about 0.1 m^3 (again limited by the size of the system's cabinet). We have achieved resolutions in the range of 250 μm.

The Medium-Energy CAT System

The MECAT system (100–700 keV) is in the system characterization and evaluation stage. A schematic of the MECAT system is shown in Figure 6. Notice that it is of the same basic design as the first-generation PBCAT system. The MECAT uses as radioisotopic sources iridium-192 (296, 308, 317, 468, and 604 keV), cesium-137 (662 keV), and cobalt-60 (1.173 and 1.333 MeV) and also a 420-keV x-ray tube source. The x rays are detected by a high-purity germanium detector. The prototype is located in a large room and can inspect objects of sizes up to about 0.15 m^3. Spatial resolutions are expected in the range of 500 μm.

Future CT Systems

We are looking for ways to improve our current CT systems. Specifically, we want to achieve higher spatial resolutions, be able to use different x-ray energy sources (different energies and intensities), and use alternate configurations for data acquisition. In addition, we are developing three new CT systems: a high-resolution vacuum micro-CT system (μCAT), a high-energy CT system (HECAT), and a planar CT system.

The μCAT system, presently in the design stage, will be used both as a microtomography system at LLNL and as a transportable setup for acquiring CT data from the high-vacuum synchrotron beamline at the Stanford Synchrotron Radiation Laboratory (SSRL). When used at LLNL, the μCAT system will use low-energy x rays and will be housed in a vacuum chamber to reduce the attenuation when imaging low-density materials in air. When used at SSRL, we will use their high-intensity monoenergetic x rays as the illuminating radiation. This system shows promise of submicron resolution.

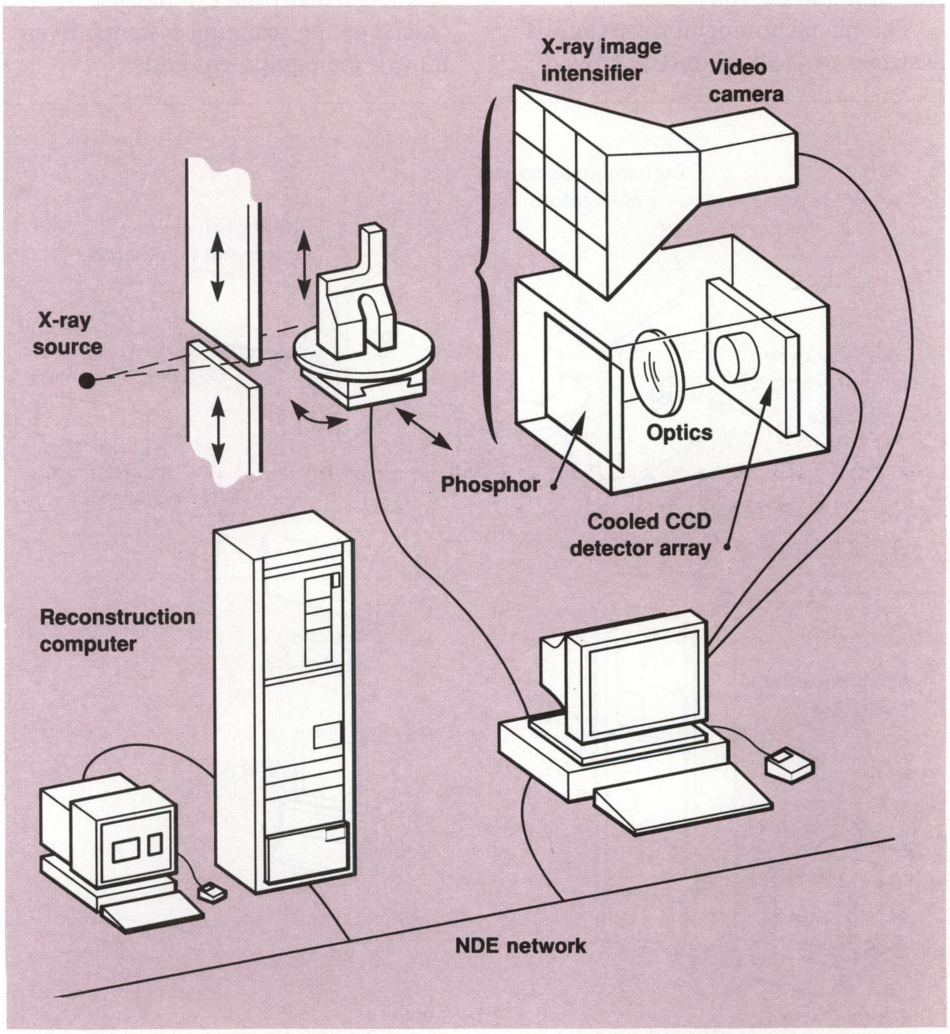

Figure 4. Diagram of the video-based CT system (VCAT). The object is illuminated by x rays in a fan or cone beam (adjusted by collimators) from a microfocus tube source. The transmitted rays are detected by two possible detector systems: an image intensifier coupled to a video system and a scintillator material optically coupled to a high-resolution two-dimensional cooled CCD array. Overall system resolution is limited by the spot size of the x-ray source and the signal-to-noise ratio of the video system.

The HECAT system, also in the design stage, will be configured to measure larger, higher-density objects with moderate spatial resolution (0.5 mm). The high-energy system will be used to evaluate closed systems, structural components, castings, and advanced materials. HECAT will use a cobalt-60 (1.173- and 1.333-MeV) radioisotopic source, and 4- and 8-MeV linear accelerators. The detector will be of a fluoroscopic design so that it can be used for real-time radiography.

The planar tomography system is designed to yield reconstructions of planar slices through flat objects from only a few two-dimensional projections. Typical objects to be inspected with this system include electronic components and metal-to-metal joints. It has been assembled, and characterization is in progress.

Algorithm Research

The image-reconstruction techniques used to interpret the data and reconstruct the CT images are as crucial as the scanning systems. Even though the equipment and instrumentation have been optimized, we can continue to improve the CT system with better algorithms. We are focusing on three areas of work: conventional (nonmodel-based) algorithms, model-based algorithms (which use *a priori* knowledge about the object itself), and parallel algorithms that exploit special-purpose processors.

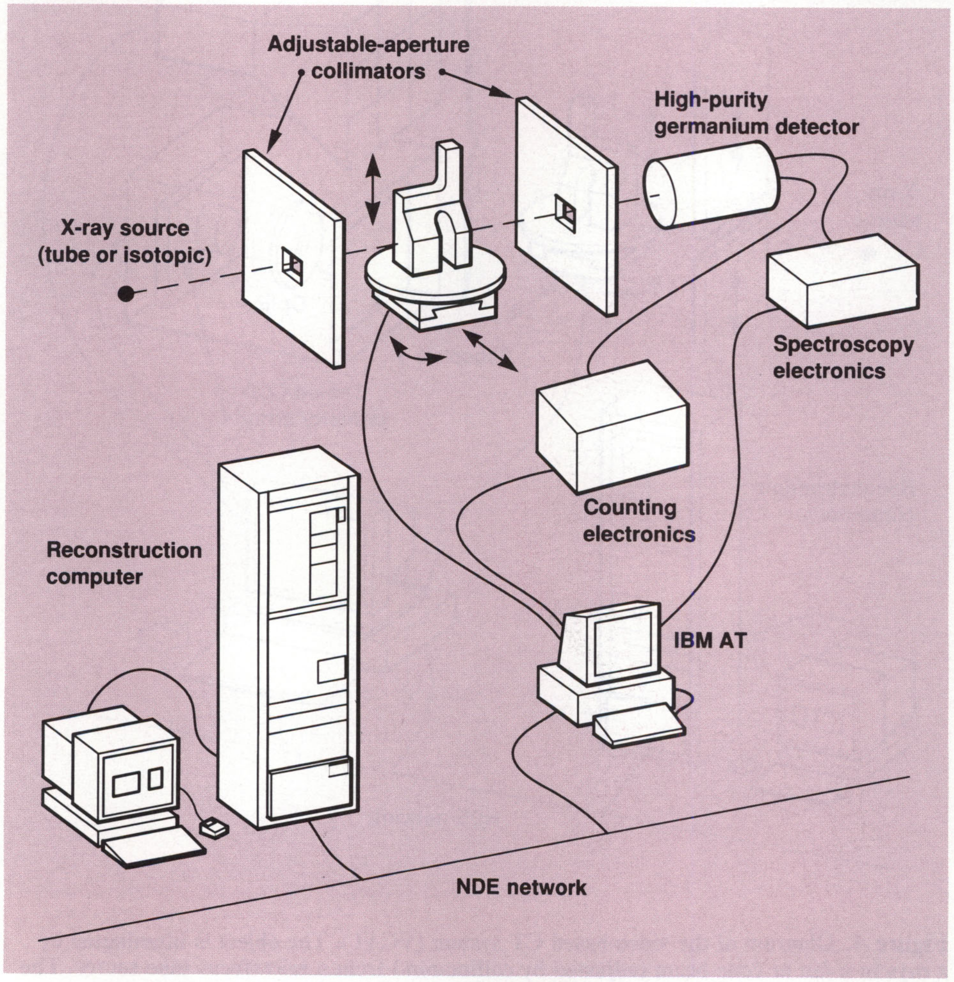

Figure 5. Diagram of the pencil-beam CT system (PBCAT). The object is illuminated with a tightly collimated beam of radiation from a radioisotope source. An intrinsic germanium detector is used in conjuction with gamma-spectroscopy electronics.

Conventional Algorithms

The traditional methods for reconstructing CT images fall into two general classes, known as transform-based and series-expansion techniques. All CT recorded data are discrete, and the distinction between transform methods and series-expansion methods has to do with the stage at which we convert from a continuous to a discrete model. For transform methods, the discretization occurs after an analytic inversion formula has been found; that is, we develop a continuous inverse Radon transform[4] and then adapt it to discrete and noisy data. In the series-expansion techniques, we first discretize the entire problem and then find the inverse transform; the approach is to express the image as a set of basic functions (usually the set of pixels) with unknown coefficients (density weights) to be found from the discrete measurements.

Transform methods. Transform methods are based on the projection-slice theorem, which simply states that the one-dimensional Fourier transform of the projection $g_\theta(s)$ with respect to s is equal to a slice through the origin of the two-dimensional Fourier transform of $f(x,y)$ at angle θ. Mathematically,

$$G_\theta(\xi) = F(\xi \cos\theta, \xi \sin\theta) ,$$

where $G_\theta(\xi)$ is the one-dimensional Fourier transform of $g_\theta(s)$ and

$F(\omega_1,\omega_2)$ is the two-dimensional Fourier transform of $f(x,y)$. This result is shown in Figure 7.

One possible reconstruction method for estimating $f(x,y)$ follows direct application of the projection-slice theorem. In this algorithm, called direct Fourier inversion, we first measure $g_\theta(s)$ at many angles θ, then take the one-dimensional Fourier transform of each of them (with respect to s) to give the value of $F(\xi \cos\theta, \xi \sin\theta)$ along many radial lines. Next, interpolate from the polar samples onto a square grid, and then take the inverse Fourier transform (two-dimensional) of $F(\omega_1,\omega_2)$to obtain an estimate of $f(x,y)$.

Unfortunately, this method, while fast, produces inadequate images compared to the backprojection techniques (described below), so it is very rarely used. This is largely because the interpolation step results in both implementation difficulties and, when not interpolated correctly, sensitivity to noise variations in the raw data.

By far the most common technique is the filtered backprojection algorithm, which is a transform method that uses the backprojection integral derived from the projection-slice theorem:

$$f(x,y) = \int_0^\pi \tilde{g}_\theta(x\cos\theta + y\sin\theta)\,d\theta,$$

where the $\tilde{g}_\theta(s)$ functions for each angle are one-dimensional filtered projections given by

$$\tilde{g}_\theta(s) = \left\{F_1^{-1}\left[G_\theta(\xi)|\xi|\right]\right\}(s),$$

where $F_1^{-1}[\ ]$ is the one-dimensional inverse Fourier transform operator.

Several variations exist of backprojection-based algorithms, which are distinguished by the nature of the filter and the order of operations. Filtered backprojection is popular because it is fast, easy to implement, and produces high-quality images so long as the number of rays and projections is high (not limited). Virtually all commercial medical CAT scanners use a variant of the backprojection methods because of the speed and image quality that these methods afford for full projections with high signal-to-noise ratios. The backprojection sum is performed entirely in the spatial domain, and special-purpose processors can be designed to make it extremely fast.

Series-expansion methods. In the series-expansion techniques, sometimes called algebraic methods, the discretization occurs at the beginning of the mathematical derivation; that is, the reconstruction area is divided into a pixelized grid. The linear properties of the Radon transform are used to develop a finite-difference model of the process. This discrete formulation leads to a linear system of equations. The solution is found numerically by solving a large sparse matrix equation, which is usually done iteratively. Then a solution concept (an optimization or

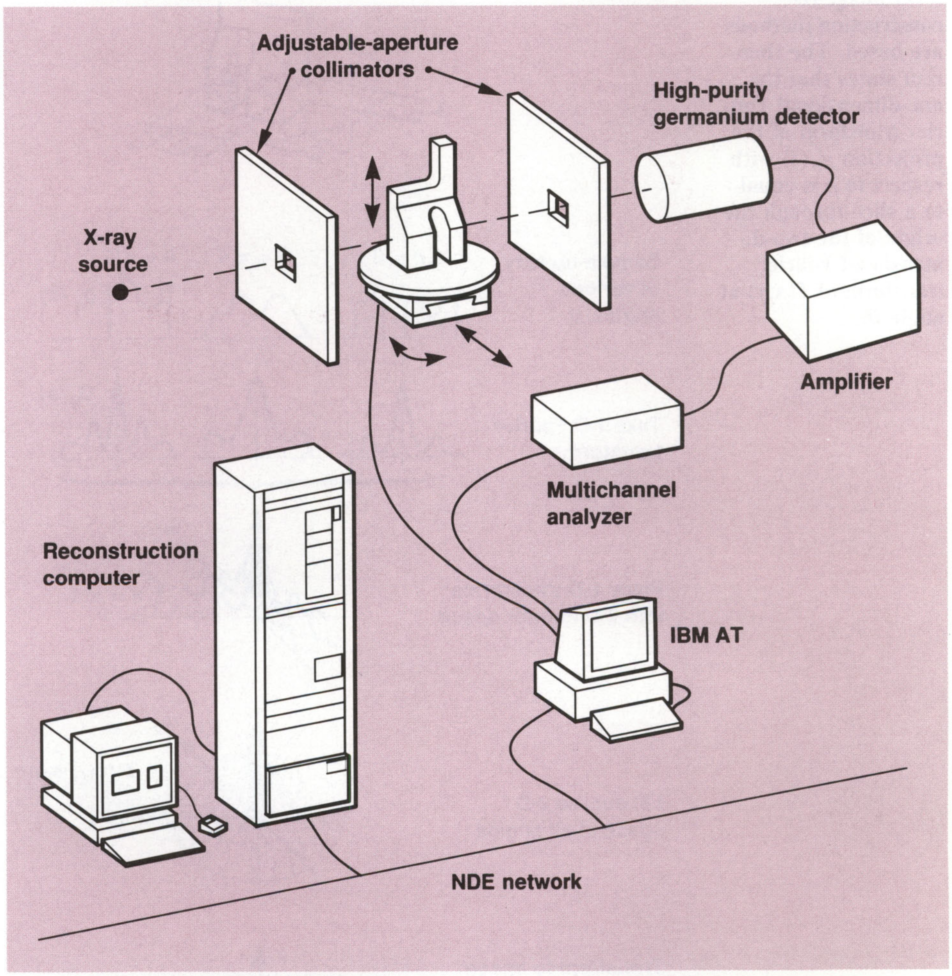

Figure 6. Diagram of the medium-energy CT system (MECAT). The MECAT will be able to use either radioisotope sources or an x-ray tube. The detector and associated electronics will be similar to those used for PBCAT.

feasibility criterion) is chosen to affect the set of possible solutions and force convergence to some answer where the error is minimized. Although usually much slower than the transform techniques (described above), the series-expansion methods can do a better job when the number of measurements is small. In addition, these iterative methods are generally more amenable to incorporating the *a priori* information discussed below. Among these algorithms are algebraic-reconstruction techniques and maximum-entropy techniques. Problems arise with series-expansion techniques because the matrix equation is usually underdetermined or inconsistent, the inversion is often slow to converge, and it is not always clear when to stop iterating.

We now have fully operational codes for both filtered backprojection and a modified series-expansion technique based on ART (algebraic reconstruction technique).

Figure 7. **The projection-slice theorem, on which the transform image-reconstruction methods are based. The theorem states that the one-dimensional Fourier transform of the projection $g_\theta(s)$ with respect to s is equal to a slice through the origin of the two-dimensional Fourier transform of $f(x,y)$ at angle θ.**

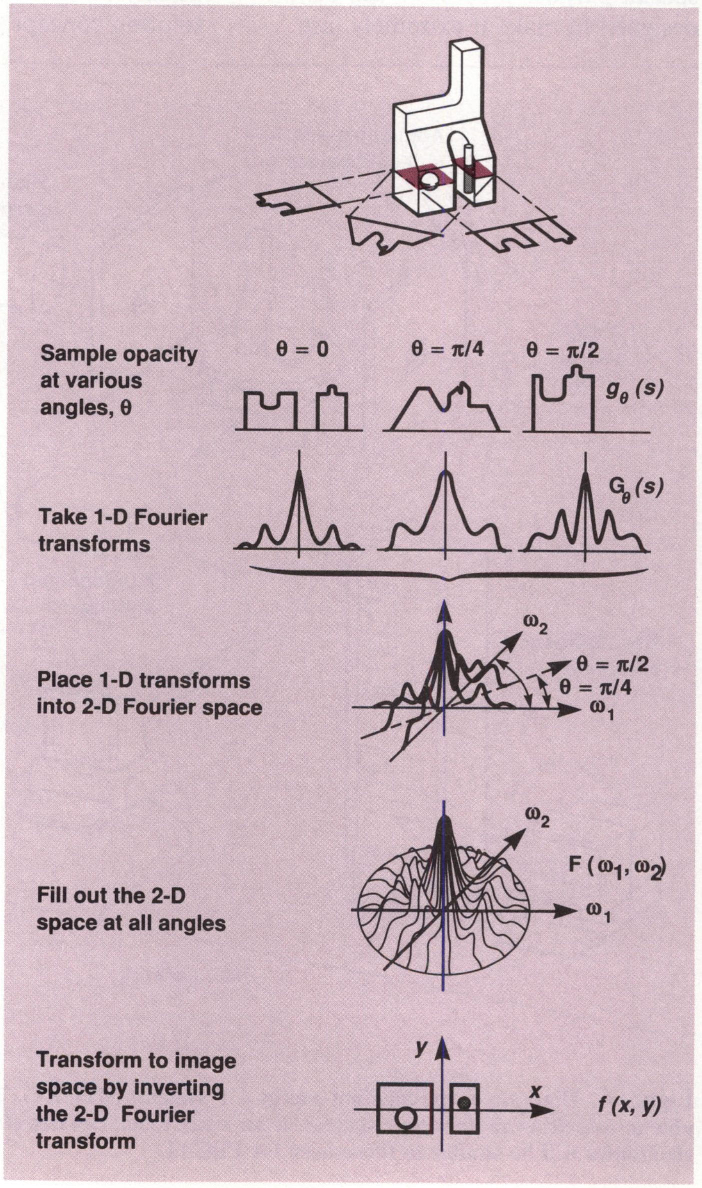

Model-Based Algorithms

All of the conventional methods described above break down when only limited data are available. However, in an industrial setting, we can often take advantage of highly accurate models of the object's shape, size, structure, and composition since these objects are often designed by computer-aided design packages whose data base is available. Incorporating these models intelligently into the reconstruction algorithms has been mentioned in the literature as another step to improving resolution and is a direction we are pursuing in our research. The alternate methods that use *a priori* information in the reconstruction of CT images, also called model-based reconstruction methods, will be useful in improving the image quality and in reducing the time required to reconstruct images (by reducing the volume of data that must be collected).

Both the transform-based and the series-expansion approaches can be modified to incorporate models, but each of these two methodologies handles limited data sets in fundamentally different ways. With transform methods, we must somehow complete the projection data in order to execute the algorithm. In contrast, the series-expansion methods essentially ignore missing data since they represent missing equations in a linear system. We find that iterative solutions of either method are generally better suited for these cases provided some *a priori* information is available.

The types of available information that can be useful in CT are summarized in Table 3. Most useful will be the object-dependent parameters that we can incorporate into the algorithms so long as they are properly aligned. These include any boundaries between subregions of differing densities and the expected densities in those regions (with tolerances), all of which can be derived from a computer-aided design data base. Other stochastic information about certain regions of the object, such as its texture and smoothness, could conceivably be included in the models as well. We may also use our expectations about the shapes, sizes, general locations, and numbers of defects in an object to improve the detection capabilities. A number of algorithms fall into the model-based class for limited data reconstructions. We surveyed some of the most promising algorithms,[7] including interpolated and extrapolated algebraic-reconstruction techniques, domain-iterative techniques, optimization methods, and orthogonal expansion. Initial results with a projection-to-image domain iterative algorithm show great improvement for the hollow- and truncated-projection problems.[8] We are actively exploring these and other novel algorithms for improvements of the resultant images.

Parallel Algorithms for Specialized Architectures

These image-reconstruction algorithms are very time consuming when performed on general-purpose computers. However, computers with specialized architectures may be able to run the algorithms fast enough to achieve reasonable reconstruction times. These computers exploit some inherent parallelism or set of operations in an algorithm that can be executed concurrently in a reconstruction technique. They have multiple computing elements that operate independently, with paths to communicate data between elements. For example, an off-the-shelf pipelined array processor attached to a workstation has been widely applied. The instruction overlap provided by the pipelining and the array capability greatly improve the reconstruction times over those possible using the workstation alone. This has been our common mode of operation at LLNL.

The backprojection and forward-projection formulas (inverse and forward Radon transforms) used in some CT image-reconstruction algorithms are well suited to implementation on a systolic array of processors.[9] One such computer, the Systolic Processor with a Reconfigurable Interconnection Network of Transputers (SPRINT) was developed at LLNL[10] and has been used to speed up image reconstruction. Each processor handles the backprojection (or forward projection) for a single one-dimensional projection angle while the image data are pipelined through them in various ways. The "rho" (or ramp) filters required by the filtered backprojection algorithms are also implemented in parallel on the processor array. The SPRINT is about 15 times faster than a VAX 8600 running the same algorithm. This configuration is particularly useful for algorithms that iterate between image and projection domains to converge on an answer. In addition, we are designing three-dimensional cone-beam reconstruction algorithms using SPRINT, which should show especially dramatic improvements in speed.

Table 3. **Possible *a priori* information used in model-based algorithms.**

Information	Common assumptions
Noise models:	
Known probability density function of all noise sources	Gaussian (mean and variance)
Correlations or covariances	Uncorrelated (white)
Independence	Independent
Shape of beam profile	Gaussian or rectangular
Shape of detector profile	Gaussian or rectangular
Global data properties:	
Consistency	$\int\int f(x,y)dxdy = \int g(s,\theta)ds$
Finite extent	$f(x,y) = 0$ beyond diameter D (so $F(\omega_1,\omega_2)$ is analytic)
Bounds	Positivity ($f(x,y) \geq 0$) and upper bound ($f(x,y) < f_{\max}$)
Bandlimit	$F(\omega_1,\omega_2) = 0$ beyond Ω
Image values	Real (so $F(\omega_1,\omega_2)$ has symmetries and periodicity)
Local features (require registration):	
Object boundaries (convex hull)	Unknown
Expected densities of subregions	Unknown
Manufacturing tolerances (bounds)	Unknown
Stochastic information (smoothness, texture, etc.)	Unknown
Symmetries	None
Defect shapes, sizes, numbers, and location	Unknown

A related project, using the SPRINT as a test-bed, involves the design of a hardware Radon Transform Computer, which has uses in many applications including CT reconstructions. It is based on the PPPE architecture proposed by Sanz, *et al.*[11] This work is a joint LLNL-UC Davis project. We expect to see an improvement of one to two orders of magnitude over the SPRINT for two-dimensional reconstructions. With enough (very inexpensive) processors, this computer should be able to run the forward and inverse Radon transforms in somewhat less than a second.

Image Analysis and Display

Once we have reconstructed images of the object of interest, we must display those images for examination and analysis. Medical CT images are usually simply displayed on a video monitor, and a radiologist adjusts the brightness, contrast, and possibly color. He can also select a line through the image and display the density values along that line. Three-dimensional renderings of multiplanar reconstructions are only now becoming available. This type of display is important in industrial CT also, as illustrated by the tomogram in Figure 8. Porosity data were collected on the PBCAT system using a spatial resolution of about 300 μm. The differences in densities, and therefore porosity, between the samples are readily apparent.

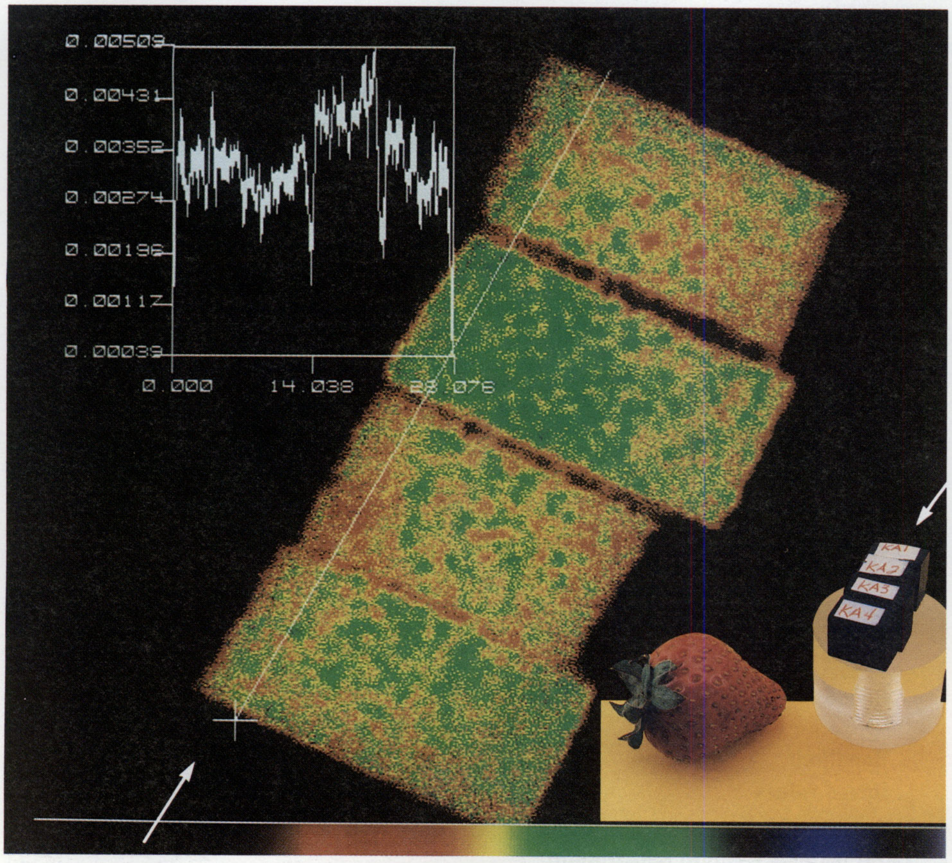

Figure 8. Reconstruction of a CT slice through a carbon-carbon composite and the density profile through a single line. This figure shows four small blocks (13 × 7 mm) of carbon-carbon composite materials at various stages of manufacture. We used CT to measure variations of porosity (which is related to the density) of the samples. The data were collected on the PBCAT system using a spatial resolution of about 300 μm. The color bar at the bottom gives a mapping of color to density. Attenuation values along the white line through the four blocks is plotted in the graph. The differences in densities, and therefore porosity, between the samples are readily apparent.

We have developed the VIEW software system[12] as a general image-processing tool and have adapted it to handle all of our CT data collection, reconstruction, and processing. The VIEW system has filtering, analysis, and display options for multidimensional signal processing. It is particularly designed for color workstations. All VIEW operations are available to the CT user.

We are also exploring three-dimensional reconstruction methods. One new way to display data is shown in Figure 9. This image is one of many views of this object (a teacup) that were pieced together into a "film-clip" for interactive viewing on the Pixar imaging computer. Note that the full three-dimensional volume of data is still available, so many imaginative displays can be attempted. The cutout technique to show internal structure, illustrated in Figure 9, is only one example of the many ways to display information about the object. Another example is translucent rendering, where different structures are displayed in different colors or with different transparency values to achieve novel effects.

We are considering other new techniques for displaying information complementary to x-ray CT. Elemental imaging (determining actual elemental makeup, not just density) can be done by performing scans at several different energy ranges and combining their information.[13] Precise control of the illuminating energy (perhaps using the synchrotron) is essential to this technique. Similar ideas for extracting information from multiple scans has also been suggested and is called multimedia CT.[14] Here, a single part is examined with different imaging modalities (e.g., x-ray vs proton radiation, low-frequency vs high-frequency, wide-band vs narrow-band). With this method, it is difficult to identify and register corresponding locations in images acquired by different instruments at possibly different magnifications and orientations. However, once these problems are solved, a large amount of new information will become available to us.

Summary

We have described the status of current and planned CT technologies for industrial inspections at LLNL. We are actively continuing to research and develop new techniques to advance the state of the art while supplying Laboratory scientists with production facilities to gather the most complete information about their materials and assemblies. We are concentrating our research efforts in the areas of scanner development and characterization, image-reconstruction algorithm development, parallel implementation of algorithms on new, fast, computer architectures, and novel data-analysis and image-display techniques. Computed tomography has become a very valuable nondestructive evaluation technique for both industry and medicine, and the utility of CT and the detail of CT imaging will continue to improve.

Key Words: algorithms—filtered backprojection, image-reconstruction, model-based, parallel, projection-slice theorem; computed tomography (CT); image analysis and display; nondestructive evaluation; pencil-beam system (PBCAT); video-based cone-beam system (VCAT).

Notes and References

1. Alternate contacts are K. E. Waltjen (415) 422-7965, or D. J. Schneberk (415) 422-6546. In addition, valuable interchanges have taken place with staff members at the University of California at Davis, BioImaging Research, ARACOR, Rockwell Science Center, Sandia National Laboratories (Livermore and Albuquerque), Jet Propulsion Lab, Exxon, General Electric, Lawrence Berkeley Laboratory, and the University of Pennsylvania. We also thank C. Grant of LLNL for the Pixar images.
2. CT was originally known as Computerized Axial Tomography (as in "CAT scanners"). It originated in medical radiography and is becoming common in NDE. A reconstructed image is called a tomogram. The prefix tomo- stems from the Greek combining form meaning "a cut" or "section."
3. G. N. Hounsfield, "Computerized Transverse Axial Scanning (Tomography): Part 1: Description of System," *Brit. J. Radiology* **46**, 1016–1022 (1973).
4. Johann Radon, "Über die Bestimmung von Funktionen durch ihre Integralwerte längs gewisser Mannigfaltigkeiten (On the Determination of Functions from their Integrals Along Certain Manifolds)," *Berichte Sächsische Akademie der Wissenschaften, Leipzig, Math.—Phys. Kl.* **69**, 262–267 (1917).
5. See the article "Quantitative Nondestructive Evaluation" in the March 1987 issue of *Energy and Technology Review* (UCRL-52000-87-3), pp. 11–21.
6. The prime collaborators at SNLL were A. J. Antolak and A. E. Pontau.

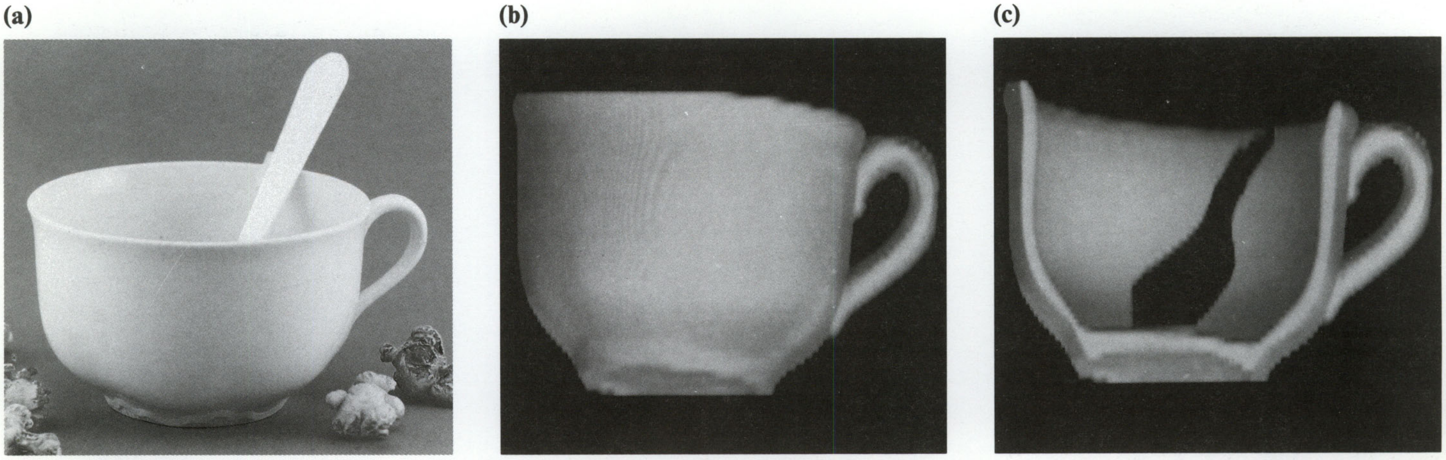

Figure 9. **Illustration of the reconstruction capability from three-dimensional data sets using the Pixar computer. (a) Photograph of a ceramic teacup. (b, c) Graphical renderings of three-dimensional multiplanar CT reconstructions. The full three-dimensional volume of data was read into a Pixar imaging computer, where it was thresholded to detect surfaces. A simulated light source was used to render those surfaces visible and generate the image. For (c), the reconstruction parameters were selected to show "internal structure" (here, a spoon).**

7. S. G. Azevedo, *Model-Based Computed Tomography for Nondestructive Evaluation,* Lawrence Livermore National Laboratory, Rept. UCID-21380 (1988).
8. S. G. Azevedo et al., *Experimental Model-Based Computed Tomography for Hollow and Truncated Projections,* Lawrence Livermore National Laboratory, Rept. UCRL-98707 (May 1988).
9. S. G. Azevedo et al., *Tomographic Image Reconstruction Using Systolic Array Algorithms,* Lawrence Livermore National Laboratory, Rept. UCRL-98708 (May 1988).
10. A. J. De Groot et al., "SPRINT—The Systolic Processor with a Reconfigurable Interconnection Network of Transputers, *IEEE Trans. Nuc. Sci.* **NS-34** (4), 873–877 (1987).
11. J. L. C. Sanz, E. B. Hinkle, and A. K. Jain, *Radon and Projection Transform-Based Computer Vision* (Springer-Verlag, Berlin, 1988).
12 J. M. Brase, V. J Miller, and M. G. Wieting, *The VIEW Signal- and Image-Processing System,* Lawrence Livermore National Laboratory, Rept. UCID-21368 (April 1988).
13. See the article "Elemental and Chemical-State Imaging" in the November·December 1987 issue of *Energy and Technology Review* (UCRL-52000-87-11·12), pp. 37–43.
14. R. Gordon, "Toward Robotic X-Ray Vision: New Directions for Computed Tomography," *Applied Optics,* **24**(23): 4124–4133, 1985.

Three-Dimensional Image Analysis for Studying Nuclear Chromatin Structure

We have developed a light-microscope-based system for acquiring cross-sectional views of cell nuclei and computer codes to analyze these images and reconstruct the three-dimensional structures they represent.

For further information contact Phillip N. Dean (415) 422-6293.[1]

Three-dimensional imaging techniques such as computer axial tomography (CAT scans) and magnetic resonance imaging (MRI) have made many valuable contributions to science and medicine by providing new or more accurate information. Typically, these techniques build up a picture of a body's internal structure by combining information from many different viewpoints and then manipulating this data to reconstruct clinically useful cross sections of the region of interest for display. We have developed equipment for gathering the same kind of data about the internal structure of intact cell nuclei, i.e., to map the locations of chromosomal domains, and we are developing the computer codes to digest and display this information.

Strange as it may seem, although the population of human chromosomes has been completely characterized, almost nothing is known about how they fit together inside the cell nucleus. (This is because the chromosomes are generally removed from the cell for study.) It seems likely that there is some definite normal arrangement, but so far no one knows for sure what it might be, or what would happen if it were accidentally changed.

Within recent years, methods have been developed for labeling domains of the chromosomes inside intact cell nuclei with fluorescent dyes.[2] We are using a special computer-controlled microscope to obtain cross-sectional views of such nuclei, and are developing an automated Quantitative Image Processing System (QUIPS) to process this information into three-dimensional images for subsequent manipulation and display. Figure 1 shows the general layout of the equipment.

Image Acquisition Method

The first step in our process is to label individual chromosomes with fluorescein stain using the hybridization technique.[3] We then stain the nucleus itself with 4′-6-diamidino-2-phenyl-indole (DAPI) to

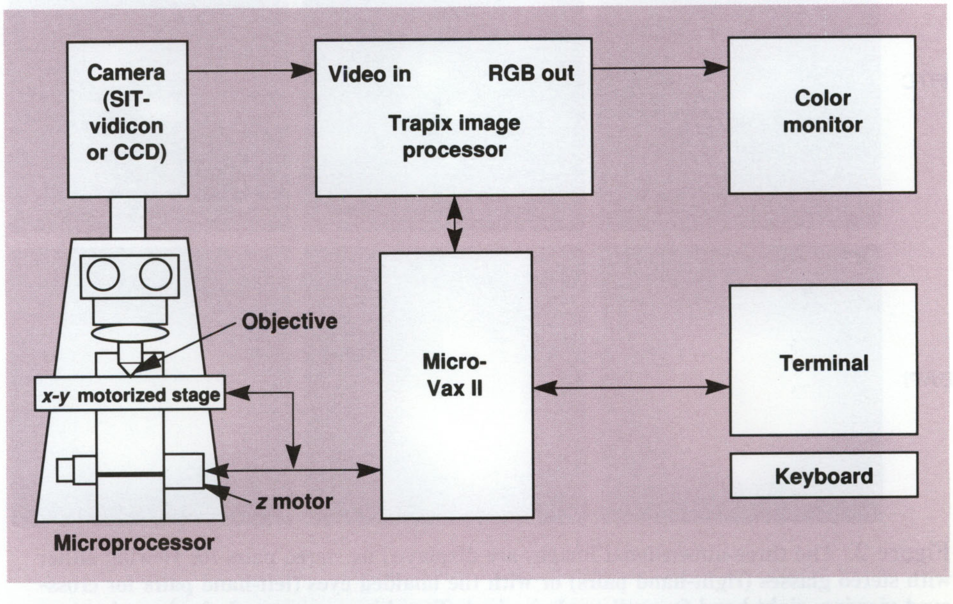

Figure 1. A schematic diagram of our Quantitative Image Processing System (QUIPS), which uses a microscope to obtain a series of thin cross-sectional views of a cell nucleus containing chromosomes stained with fluorescent dyes. The computer system digitizes each image and stores it for later analysis. By correlating data from the various images, the analysis will produce three-dimensional images that show how the chromosomes are arranged in the nucleus.

mark the extent of the DNA within it. Each of the stains yields a different color of fluorescence, making it possible to distinguish the various labeled parts. We use optical filters to view one stain at a time to further simplify image reconstruction.

To view the stained nuclei, we use a fluorescence microscope whose objective lens has a very large (1.4) numerical aperture, which gives the microscope a very shallow depth of field (about 0.5 to 1.0 μm for visible wavelengths). The result is essentially a cross-sectional view, since everything above or below this thin slice is out of focus. A computer-controlled stepping motor moves the microscope focal plane down through the cell to view successive slices through the same nucleus.

Rather than photograph each slice image, we collect it directly on the silicon-intensified target (SIT) of a vidicon camera for immediate digitizing by a Trapix image-processing unit and storage in the MicroVAX II computer that controls the entire system. The MicroVAX II analyzes the different two-dimensional images, correlates information from all of them, and builds up a three-dimensional image in its memory for later processing, display, and analysis. This process is called optical sectioning.

A necessary feature of the system is a three-dimensional image display, which helps us verify that everything is working properly. The one we use quickly creates a stereo pair on the monitor for viewing through stereoptic lenses or with the unaided eyes (Figure 2).

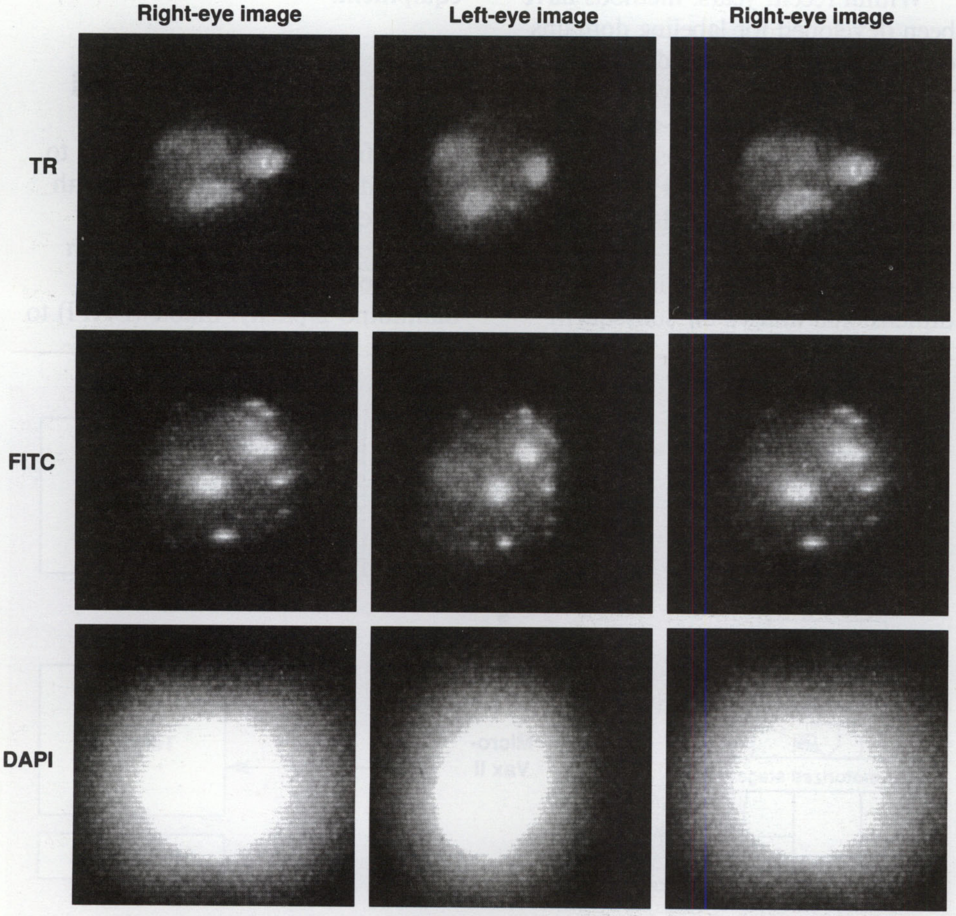

Figure 2. The three-dimensional images are displayed as stereo pairs for viewing either with stereo glasses (right-hand pairs) or with the unaided eyes (left-hand pairs for cross-eyed viewing, right-hand for wall-eyed viewing). To achieve cross-eyed viewing, place your finger between two of the leftmost images and concentrate on it as you move it toward your eyes. The images will appear to move toward each other and will eventually merge. Relax and keep the images merged while you move your finger out of the way. The images will come into focus, and you will see the three-dimensional image.

Quantitative Analysis

The first step in analyzing the image is to define the parameters needed to describe the object depicted. Figure 3, representing a slice through a nucleus, indicates the parameters that are of interest in our study. Taken together, these parameters enable us to make a precise three-dimensional map of the cell's nucleus:

- The location of the center of the nucleus, which is used as a reference point, and the location of the center of each chromosome region.
- The volume of the nucleus and of each chromosome region.
- The surface area of the nucleus and of each chromosome region.
- The shortest distance from the center of each chromosome region to the surface of the nucleus.
- The shortest distance from the surface of each chromosome region to the surface of the nucleus.

To extract this quantitative information, the system must perform several steps. It must clearly distinguish which parts of each three-dimensional image represent real constituent objects. It must then identify each of these objects and measure its features.

Some day it may be possible for a computer to perform object discrimination unaided, but for now we work interactively with QUIPS in this step. For each nucleus, we start with the images of the DAPI stain to identify the extent of the nucleus in each slice. This is achieved by selecting a fluorescence threshold (emission intensity) that separates the nucleus from the background. Each volume element (voxel) in the three-dimensional image that has an intensity greater than the threshold value is then set to 1 (that is, it lies within the nucleus). All other voxels are set to 0 (outside the nucleus). This forms a "binary" image of the nucleus. This procedure is repeated for each fluorescent probe used to label the chromosome regions. All of the binary images (e.g., as shown in Figure 4) are stored in the computer.

Next the computer locates all the objects within the three-dimensional image. To do this it looks for a filled voxel (value = 1) that has not yet been labeled as part of an object (a "seed" voxel), gives it an object number, and then searches for filled neighbor voxels (i.e., voxels that belong to the same object). To save time, the computer defines neighbor voxels as those that lie directly above, below, or to the right, left, front, or back of the seed voxel, and ignores those that touch only at the edges or corners. (This eliminates more than three-quarters of the possible connected voxels from consideration, without significant loss of accuracy for our purposes.) It repeats this process for each filled neighbor voxel until it finds all the filled voxels connected to the original "seed" voxel. Then it searches for another filled voxel that is not part of the first object and repeats the process.

At the same time that the computer is finding the voxels inside the object, it is also identifying those that lie on its surface. These are the ones that have an empty neighbor on one or more sides.

From these measurements, the computer calculates the various parameters of interest for each object. The volume calculation is straightforward: the number of voxels that are within the object.

Calculating the object's center of mass is a little more complex; the computer must calculate the average moment of all the voxels about each of the three axes *x*, *y*, and *z*. It does this by multiplying the distance to each row of filled voxels from the

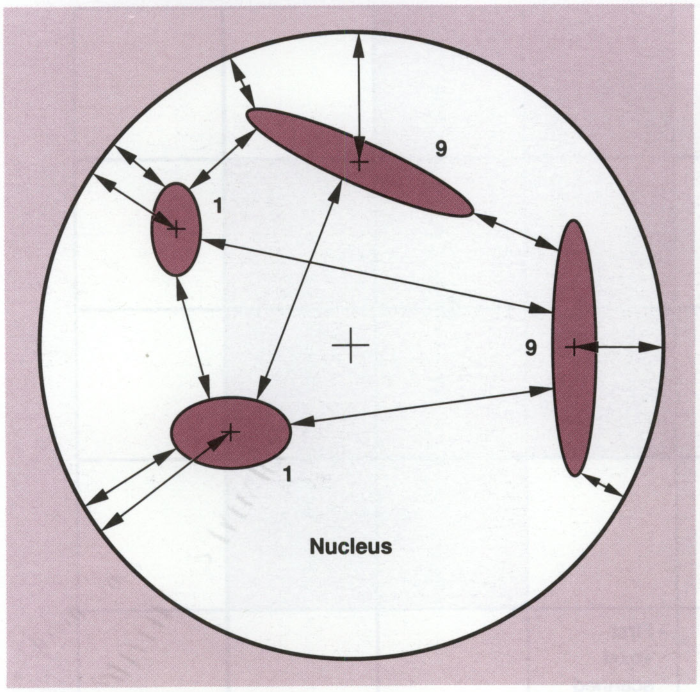

Figure 3. A cross section of a nucleus containing two pairs of chromosomes, showing some of the parameters we measure to create a three-dimensional description of their shapes and placement. Each human cell contains 46 chromosomes, 22 pairs plus two sex chromosomes (X and Y). The chromosome types are numbered to distinguish them from one another. The ones in this illustration are chromosomes 1 and 9.

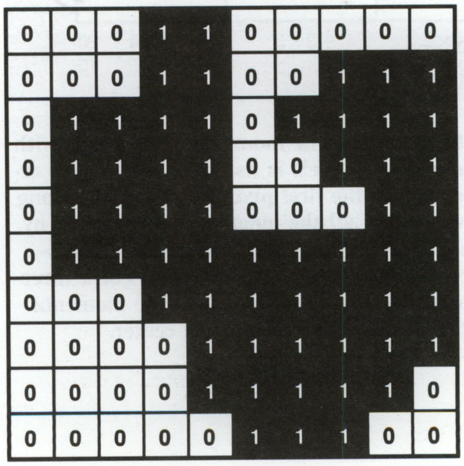

0	0	0	1	1	0	0	0	0	0
0	0	0	1	1	0	0	1	1	1
0	1	1	1	1	0	1	1	1	1
0	1	1	1	1	0	0	1	1	1
0	1	1	1	1	0	0	0	1	1
0	1	1	1	1	1	1	1	1	1
0	0	0	1	1	1	1	1	1	1
0	0	0	0	1	1	1	1	1	1
0	0	0	0	1	1	1	1	1	0
0	0	0	0	0	1	1	1	0	0

Figure 4. A two-dimensional example of object discrimination by thresholding. Any pixel in which the fluorescent light intensity is above a set threshold is considered "filled," and the bit representing it in the computer's memory is set to a 1. Pixels below the threshold are empty; their bits are 0.

origin (the first voxel scanned) by the number of filled voxels in that row, adding all the moments, and dividing by the number of voxels (Figure 5). This gives one coordinate of the center of mass; repeating the process for the other axes provides the other two coordinates.

Surface area is the most difficult parameter to calculate; it is not just the sum of surface voxels because each voxel has the same volume but one of them may represent several times as much area as another. Instead we have to classify each surface voxel according to its neighborhood configuration (Figure 6) and then assign areas to each configuration. Later on, we can vary these area assignments on the basis of experience to yield the best approximation to an object's true surface area.

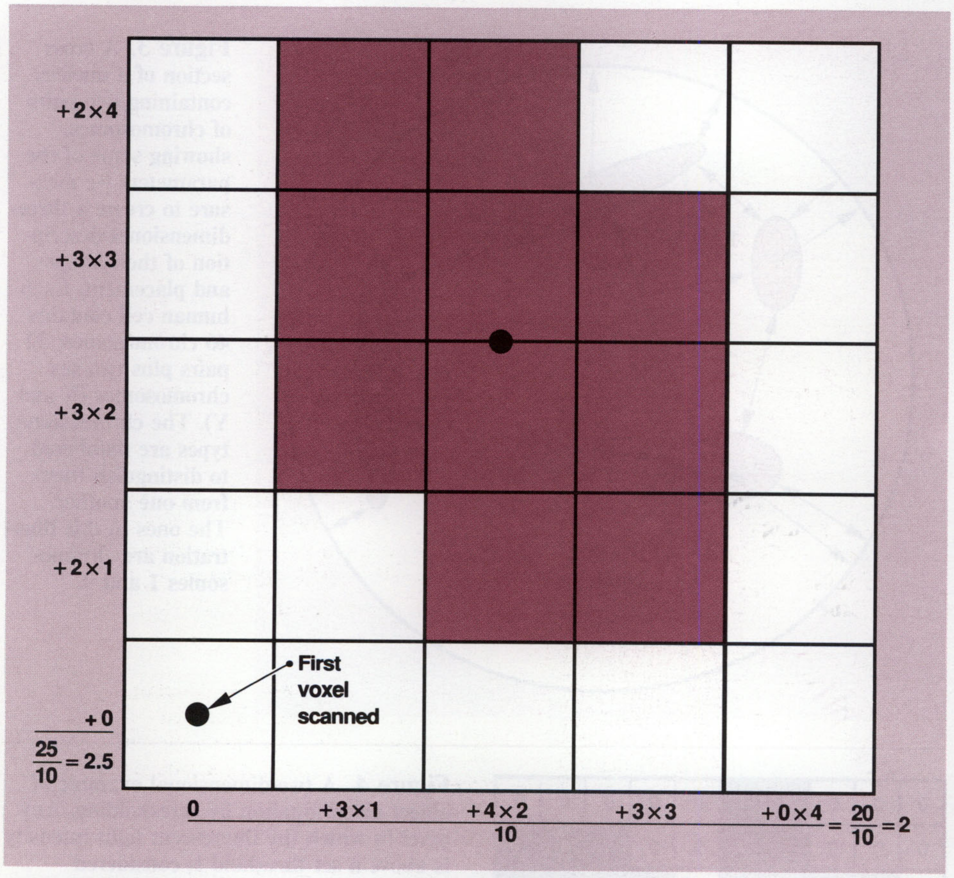

Figure 5. Locating an object's center of mass by averaging the moments of its pixels with respect to the *x* and *y* axes. The moment for each row of pixels is its distance from the origin (the point through which all the axes go, located in the first pixel encountered), along the *y* axis times the number of pixels in the row. Adding all the moments and dividing by the number of pixels gives the distance from the *x* axis to the center. Repeating the process for each column of pixels gives the distance from the *y* axis to the center. For a three-dimensional object, the whole procedure is repeated for each slice and then the momenta for all the slices are averaged to obtain the distance from the *z* axis to the center.

To economize on computation time and memory requirements in measuring distances inward from the surface of the cell nucleus to the chromosome surfaces and centers, we use a distance transform that tabulates the distance from each voxel in the nucleus to the nearest voxel on the nucleus surface. To determine how far it is from a chromosome's center to the nucleus's surface, once it finds which voxel contains the center, the program looks it up in the distance table. Similarly, it can find the minimum distance between the chromosome surface and the nucleus surface without further computation by comparing the tabulated distances for all the chromosome's surface voxels.

Testing the Algorithms

To test the accuracy of ANA-3D, our algorithm for determining surface area, center of mass, and volume, we ran a number of computer simulations using spheres of various sizes. We let the true center of the sphere fall randomly within the center voxel, and then picked out the "filled" and "empty" voxels according to whether the voxel center is inside the sphere's surface or outside (Figure 7).

We ran simulations using sphere radii of 2, 3, 4, 5, 7, 10, 14, 20, 28, and 40 voxels, and for each radius we analyzed 25 random cases. Since the true values of volume, surface area, center of mass, and the like are known for a sphere of any size, we could then determine how many sections our algorithm would need to estimate these parameters to within a given accuracy.

As might be expected, the more voxels we use to define a sphere, the more accurate our estimate of sphere volume becomes. For spheres more than five voxels in radius (a sampling interval of at least 10 voxels across the sphere), we can expect the calculated volume, on the average, to be within 1% of the true volume. Similarly, the mean center-of-mass radial error (the radial distance between the true center and the calculated center, averaged over a number of trials) is quite low even for small objects. At a radius as small as two voxels, one standard deviation above the mean of the radial error for 25 cases is less than 10% of the sampling interval.

The calculation of surface area is much less certain. Figure 8 shows how the error varies with radius for four different measurement schemes. In the best of these methods, the error is never more than 3% and it rapidly diminishes for larger spheres. However, this method may be best only for spheres; for a cube its answer would be 33% low. Clearly this is a field requiring further development.

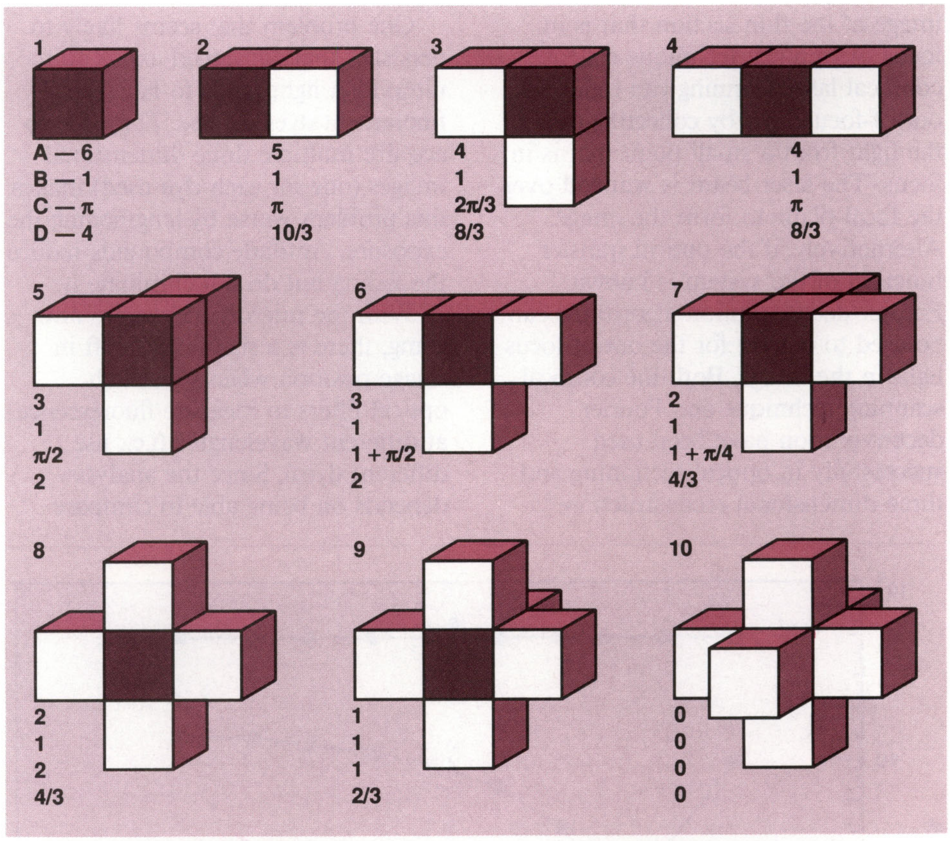

Figure 6. Ten unique configurations of filled voxels around a central voxel. (Symmetry is assumed; turning or reflecting one of these shapes does not change the exposed area of the colored voxel.) For surface area calculations we assign a numerical (weighting) value for each of these shapes. We have evaluated several different weighting schemes, four of which (labeled A, B, C, and D here and in Figure 8) are tabulated below each image.

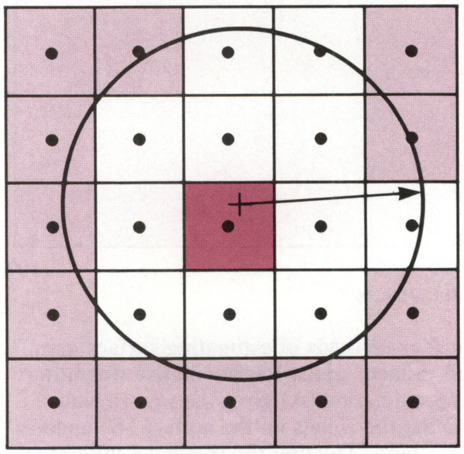

Figure 7. To test the accuracy of our image-processing algorithms, we measure the parameters of randomly placed spheres of different sizes. We assign a voxel for inclusion in the sphere if its center lies within the sphere (white voxels). The center of the sphere could be anywhere within the colored (central) voxel.

Problems of Data Acquisition

Before we can reliably apply our ANA-3D algorithm to chromosome measurements, we must surmount several problems created by the equipment that can compromise the accuracy of the data collected and can introduce unknown magnitudes of error in any analysis. For all but one of the major problems, there are proven or potential solutions.

When using conventional epifluorescence microscopy, the entire nucleus is exposed to ultraviolet light. Fluorescence light coming from areas outside the focal plane will blur the image of the thin section that is in focus. An optical technique called confocal laser scanning can reduce the out-of-focus light by collecting only the light from a small point that is in focus. The laser beam is scanned over the focal plane to form the image. Alternatively, if the optical transfer function of the system is known, Fourier deconvolution algorithms can be used to correct for the out-of-focus light in the image. Both the confocal scanning technique and Fourier deconvolution have been used successfully in optical sectioning and three-dimensional reconstruction.[4]

One problem that seems likely to persist is that continued exposure to ultraviolet light tends to fade the fluorescent dyes we use. The need to acquire multiple three-dimensional images (one for each dye used) makes this problem worse by lengthening the exposure. Antifade compounds reduce the fading but do not eliminate it.

With the microscope we are now using, there is a significant shift in image position when we switch optical filters to measure fluorescence at different wavelengths (i.e., use different dyes). Since the analysis depends on being able to compare data from all the images, we must either eliminate this shift or allow for it in the computations. Currently, we measure the image shift and correct for it to within 0.25 μm.

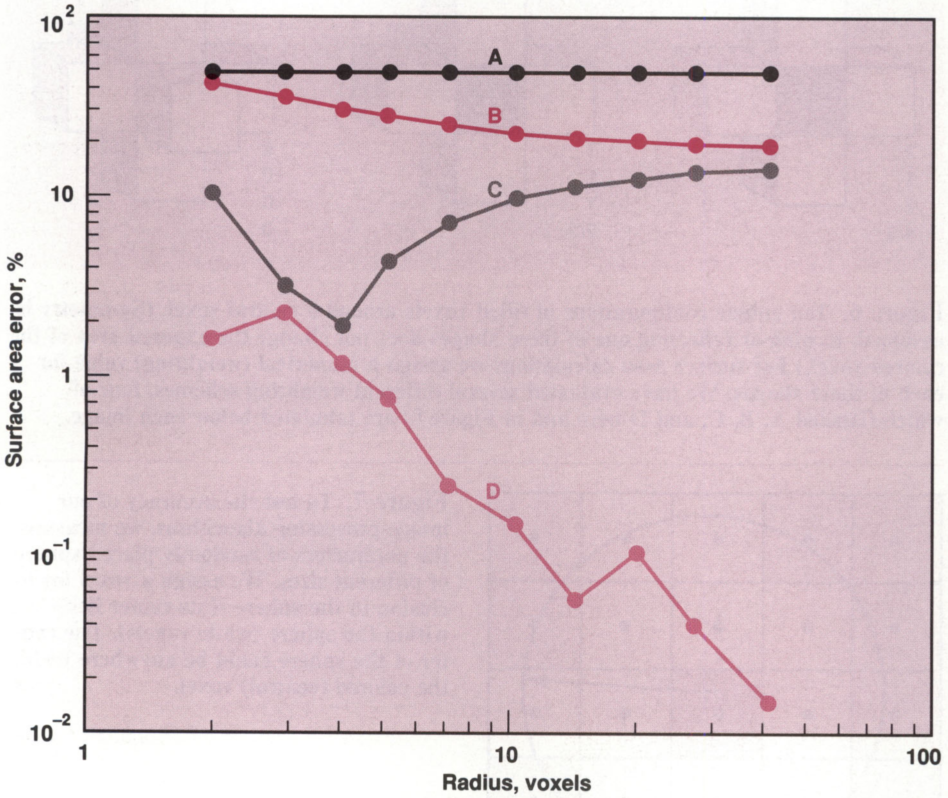

Figure 8. **A plot of absolute error vs radius for four methods of estimating surface area. Each point is the mean surface-area error for 25 random trials. Representative weighting schemes are tabulated in Figure 6. The cubic approximation (A) gives the worst result, consistently overestimating by about 50%. Summing the voxels on the surface (B) underestimates the area, approaching 20% error for large radii. Treating the voxels as spheres (C) underestimates small spheres and overestimates large ones. Dividing the cubic-approximation weights by 1.5 (D) gave the best result, 3% error for the smallest radii and rapidly diminishing error for larger radii.**

The emissions from some of the fluorescent dyes we use are so weak that they require the use of a very sensitive detector. We can adjust the gain of our SIT-vidicon camera to increase its sensitivity, but this also increases the electronic noise background. One solution would be to substitute a camera using a cooled charge-coupled device (CCD), which has excellent sensitivity and a very low signal-to-noise ratio. A confocal scanning laser microscope does not have this problem since its detector is a high-gain photomultiplier.

Future Work

One objective of our research is to measure the distances between objects (chromosomes) in the nucleus. The shift in image location with a change in optical filters continues to be a problem. Since we can estimate the center of an object to within a fraction of a voxel (for spheres with radii as small as two voxels), the present 0.25-μm uncertainty in image registration is acceptable in our present system (where the typical voxel is 0.6 μm on a side). However, if we increase the sampling density (reduce voxel size), we will need to improve the registration accuracy.

Calculation of surface area will always be a problem. We need to run many simulations with various other shapes (cylinders, cones, etc.) at random orientations and placements to further test the accuracy of our surface-area estimation methods. Depending on the results of these further tests, we may need to modify or replace the algorithm used.

We also need simulations to test the accuracy of our routines for measuring the distances between chromosome surfaces. Because of the quantity of complex data involved in these measurements, we can already see a need to modify our data-storage structures for greater speed and efficiency.

We may also find it useful to measure the total area over which two objects remain within a given minimum distance. This might prove useful in determining whether close proximity of certain chromosomes is related to disease.

All the algorithms described so far assume that the voxels are symmetrical (cubes, for example). This is not necessary; changing to asymmetric voxels could lead to valuable improvements in performance. For example, the level of detail we can resolve in each horizontal plane is much finer than the depth of the focus plane, even for a confocal scanning microscope. Therefore, fewer asymmetrical voxels (longer in the *z* direction than in the *x* and *y* directions) than cubic voxels are required to cover a nucleus. This could also be of benefit where fading of the fluorescent dyes is of concern; fewer optical sections would shorten the exposure time.

The algorithms used for measuring volume and center of mass can be easily adapted to asymmetric voxels. Those used for computing surface area and for the distance transform, however, would need to be modified substantially and thoroughly tested for accuracy.

Computer programs used for image processing and analysis make enormous demands on computer memory and computational speed. Doubling the sampling density increases the memory requirement by a factor of eight. At eight bits per voxel, a single image 128 cubes on a side requires 2 Mbyte of memory; at 16 bits per voxel, three images of the same cell and its distance transform image raise the memory demand to 16 Mbyte, not counting allocations for other variables and arrays.

The speed requirements for three-dimensional image processing and analysis favor computation-efficient algorithms that reduce processing time. We developed our routines with this in mind. For example, once an object has been identified, only voxels that are part of it are processed and stored, making it unnecessary to re-scan the image. This technique is efficient for images in which the constituent objects occupy less than half the total image space. Nevertheless, despite the efficiency of our algorithms, the sheer size of the three-dimensional images imposes substantial processing times.

For example, calculation of the parameters of interest on two $64 \times 64 \times 32$-voxel images of a cell nucleus containing two chromosomes took about 75 s of CPU time on a Motorola 68000 computer running at 12 MHz. Most of this time was spent identifying the large nucleus and calculating the distance transform. Newer workstations are up to ten times faster, and mathematics coprocessors can increase the speed of some calculations by a factor of up to 200.

Our next major goal is to apply our methods to experimental data. To determine whether the cell nucleus has an identifiable structure, quantitative analysis will have to be performed on a large number of cells. Even with faster computers and more efficient algorithms, the time and effort required to analyze these data will be considerable. However, the potential gain in knowledge of nuclear structure and its relation to genetic disease is worth the effort.

Key Words: cell nucleus; chromosome; distance transform; fluorescence hybridization; image analysis—computer-assisted, three-dimensional; optical sectioning.

Notes and References

1. James Mullikin, a major contributor to this effort, is presently on educational leave, pursuing a Ph.D. at the Delft University of Technology, Netherlands.
2. B. Trask et al., “Fluorescence In-Situ Hybridization to Interphase Cell Nuclei in Suspension Allows Flow Cytometric Analysis of Chromosome Content and Microscopic Analysis of Nuclear Organization,” *Human Genetics* **78**, 251–259 (1988).
3. “Fluorescent Labeling of Human Chromosomes with Recombinant DNA Probes,” *Energy and Technology Review* (UCRL-52000-85-7), pp. 84–85.
4. D. Agard, “Optical Sectioning Microscopy: Cellular Architecture in Three Dimensions,” *Ann. Rev. Biophys. Bioeng.* **13**, 191–219 (1984).

Imaging in the Nuclear Test Program

Advanced imaging techniques, developed at LLNL, produce images of unprecedented detail and resolution from diagnostic data obtained in experiments at the Nevada Test Site.

For further information contact Eric Frerking (415) 422-6942.

Much of the data obtained from device diagnostics at the Nevada Test Site (NTS) is produced in the form of images. Several experimental methods are used to generate and capture light images from the various radiations emitted from a nuclear explosion. These data must be generated, sent uphole to a receiving trailer, and captured in the harsh local environment of a nuclear explosion.

This article describes the role of imaging techniques used in our major image-producing experimental hardware—electronic PINEX and streaking cameras. These techniques are applied to all phases of the related experiments, including camera construction, calibration, data capture, and final image processing.

Electronic Pinhole Experiments

Just as with a classical pinhole through which a light image can be focused onto a screen, we have designed electronic pinhole experiments (EL-PINEXs) through which an image of a radiation source (primarily neutrons) can be focused by a special pinhole onto a screen made of a material that converts the radiation to light.

Cameras that are shielded from stray background radiation view this light (Figure 1), then form images on a solid-state chip that digitizes the light intensity falling on each spot of a 100 × 100-element array. Each spot on the array is represented, at this point, by a number that is proportional to the brightness of light at that spot. These digitized data are then transported via high-quality coaxial cable (or optical-fiber cable) to a receiver in an uphole trailer. The receiver captures these numbers and stores them in nonvolatile memory. This entire sequence of events must be completed within several milliseconds after an event, because the arrival of the shock wave from the event destroys all of the equipment residing downhole. The system that captures and stores the data is called the Integrated Data Acquisition (IDA) system.

After the data are safely stored in local memory in the uphole trailer, a reentry team enters the trailer and, among many other tasks, copies the data to a permanent magnetic diskette. This diskette is then carried to the NTS control point, where additional copies are made. The original information is stored in the recording trailer memory until the data have been reviewed and it is determined that no information has been lost or ignored in the transfer process.

Streak Camera Data

We are also increasing our ability to build and field streak cameras that can provide important time-dependent information about device

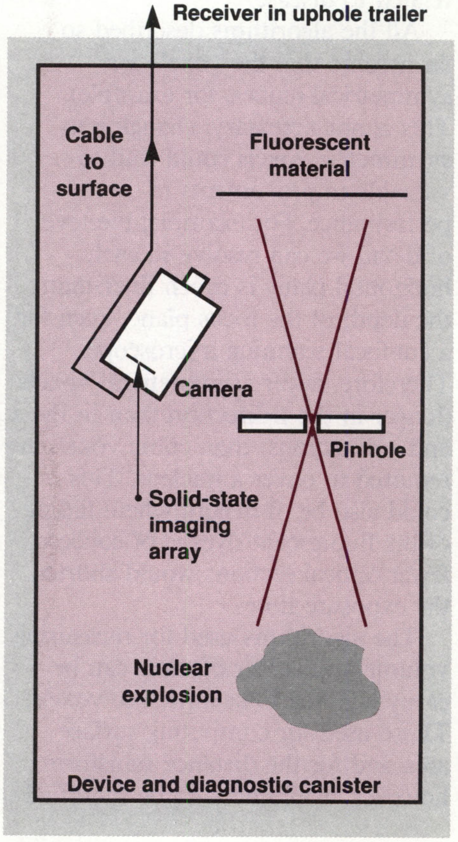

Figure 1. **Schematic diagram of the elements included in the EL-PINEX experiment. Radiation particles from the source pass through a thick pinhole, generating light at a fluorescent material at the image plane. Solid-state cameras capture the image and send the data uphole to receiving equipment in a trailer.**

behavior. Advances in streak camera technology and our ability to apply this equipment in the field have allowed us to design a number of new experiments. We can now acquire several types of data with unprecedented time resolution. Some of these methods are described below.

Since we began to record data on nuclear tests, we have used oscilloscopes to capture and record fast data. Over the years, the data bandwidth recorded by the oscilloscopes has been extended to about 1 GHz; yet the long cables required to carry signals to the scopes and the limited bandwidths of electronic systems still combine to disperse the signals to the extent that difficult deconvolution techniques must be used to extract the information of interest.

Streak cameras have system bandwidths that are much better than those of the cable-oscilloscope system. One reason for this is that the analog data need not be sent through significant lengths of electrical cable; for example, one can modulate a pulse of light with the high bandwidth analog signal so that its brightness at a given time is proportional to the analog signal amplitude at that time. This modulated signal may then travel through fiber-optic cables and be recorded as a streak on a streak camera (Figure 2), the brightness of the final streak being proportional to the original signal. Since many such streaks may be deployed on a single camera, one camera can record many channels of data from various detectors. In this way, one streak camera can replace many oscilloscopes and at the same time provide higher quality high-bandwidth results that are much easier to process and analyze.

As the camera is streaked, it produces an image of the streak that is digitized by another type of solid-state chip. This chip is larger than the EL-PINEX chip; it collects 400 × 120-element arrays. Data are sent uphole, captured, and retrieved in much the same way that the EL-PINEX data are handled.

Camera Construction and Calibration

The preparation phases for cameras that perform these sophisticated experiments are far from trivial. When data taken with these instruments are interpreted, various spatial distortions and intensity transformations can again conspire to degrade the results. Therefore, great care is taken during the construction of these cameras to understand the behavior of each component. Over time, we have developed benchmarks and criteria relating to linearity and spectral responses for the acceptance of components in a completed instrument. Even during the

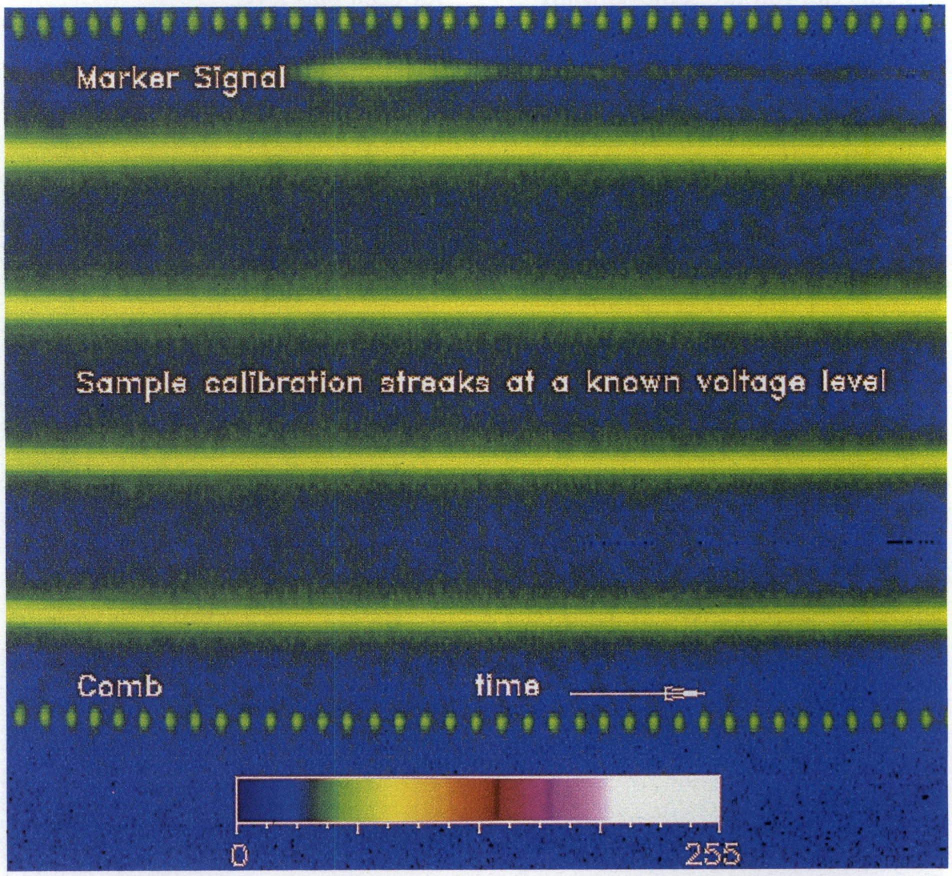

Figure 2. Each streak in this image represents a constant known voltage, thus allowing us to calibrate data to real physical units (in this case, volts). Included in this image are the comb streaks, which define a time base for the signals, a timing marker, which defines timing relative to other elements of a major recording system, and four constant-voltage streaks. The color bar shows how data values ranging from 0 to 255 are assigned a color (from left to right). Any combination of 256 colors may be chosen, as shown in the remaining figures.

construction and evaluation phase of a camera, imaging techniques play a key role.

Nearly all of the camera construction and testing is done by the Edgerton, Germeshausen, and Grier Corp. (EG&G) at facilities in Pleasanton, California, and Las Vegas, Nevada. Each of these facilities owns several image-processing systems that are nearly identical to those used in our L-Division Image Research Laboratory (LIRL) but are based on the MicroVAX II rather than on our older and slower VAX 11/750. These systems can run the same software packages and are capable of equally sophisticated processing.

One of the steps needed to adjust a camera is to set bias levels such that real signal levels do not drive the imaging chip beyond its range. To do this, one must manually adjust the setting while watching an image resulting from a constant intensity level (flat field) on the screen as it approaches a desired level. Several years ago, each bias setting required an image to be captured and an analysis done to determine the mean values and standard deviations of the image. This cycle took tens of minutes and was repeated many times for each bias level.

Our current procedure, developed at EG&G, for setting these levels is much quicker and more efficient. At each bias adjustment change, data are captured and quickly displayed with a color table, as shown in Figure 3. If the active bias level is too low, the image shows as a dull yellow. Likewise, a high setting results in a bright yellow image. As the adjustment approaches the desired value, the color becomes brown, until bright green (which represents the desired level) appears. The remaining task is then to balance and optimize the yellow, brown, and green levels by eye, because these constant-intensity or flat-field images are never really totally "flat." This entire adjustment cycle takes only a few minutes. If another level setting is desired, the color table is centered about the new level, and the new adjustment is performed. Imaging techniques such as these have made the camera setup phases much faster and more accurate than was possible before powerful and interactive image-processing methods existed.

Another part of the calibration process for a camera involves recording a sequence of flat-field images at known constant illumination levels, covering the entire range of values that real data might occupy. This allows the real data to be related to the known exposure levels of the active elements of the chips and thus be related to real physical units of the original source that generated the image. In the past, this linearity measurement was done by obtaining the overall image averages of each member of a set of flat fields, and then making a graph of these mean values vs the exposure level. Deviations from a good linearity appeared when there were problems with camera quality. With our current systems, it is easy to treat each picture element (pixel) of the set of flat-field images as a separate

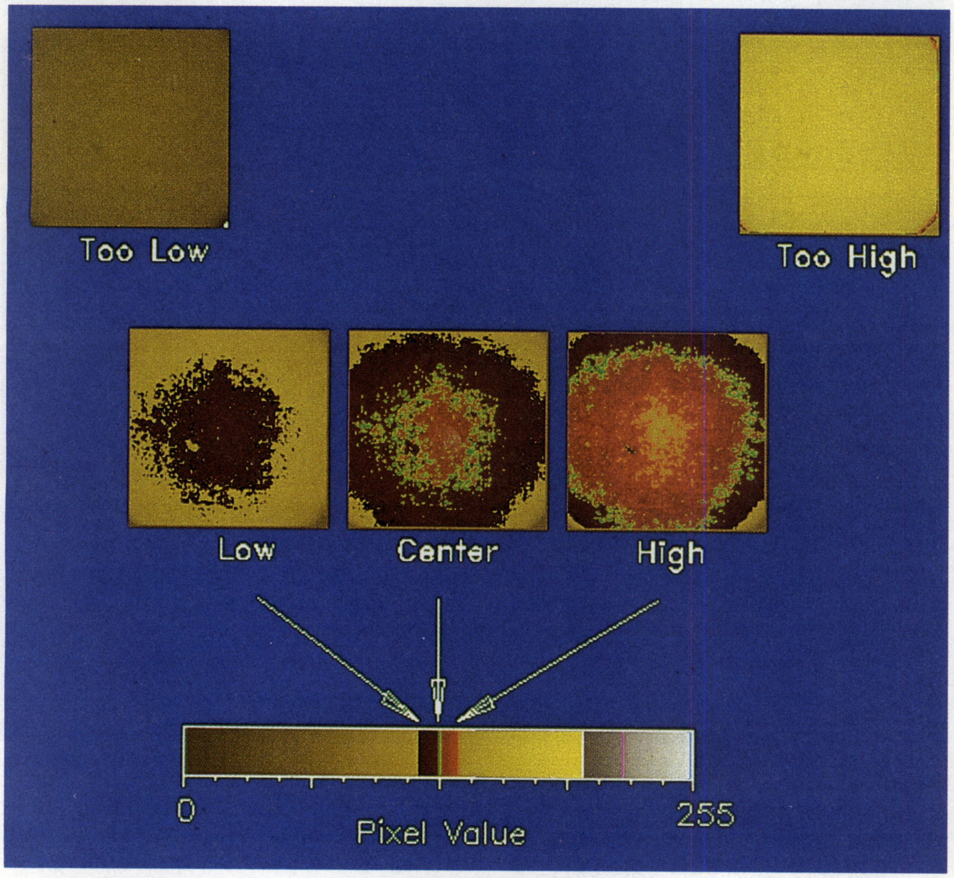

Figure 3. This color table and images demonstrate the setting of a bias level on a solid-state camera. The white pixels represent the desired level while green is low and red is high. As the desired level is approached, the colors become brighter.

linearity curve, and thus perform a pixel-by-pixel calibration of the final data image.

L-Division Image Research Laboratory

After event data are captured and previewed at NTS, they are sent via secure communications link to the LIRL facility at LLNL, along with final camera calibrations. Detailed image processing and high quality hardcopy of images are produced at LIRL for publishing of experimental results.

The LIRL consists of a VAX 11/750 computer with standard peripheral units and a number of display units that are capable of 512-element by 512-element display. Each element can be displayed with 8 bits (255 levels) of intensity that are assigned according to a 255-element table of colors. This procedure allows all of the different possible data values to be displayed with a specific color, permitting a very wide range of data displays.

LIRL is a multiuser facility, allowing several users to analyze and display data at once. Thus, users with totally different imaging applications can simultaneously use the system. Furthermore, the LIRL system makes use of two independent imaging software packages. One of these, called the LIRL package, was written by LLNL personnel; it contains no proprietary software. This package allows users to quickly view data, perform simple mathematical operations on the images, and generate various displays. The other package is a very powerful and flexible licensed commercial package, Interactive Data Language (IDL), that enables users to develop new processing techniques. In addition, IDL includes sophisticated imaging tools such as image Fourier transformations and convolutions. All of these capabilities are used extensively in the processing of event data.

Data Processing at LIRL

Once the event data reach LIRL, spatial and intensity distortions are removed from the data (EL-PINEX and streak camera) so that images closely represent the real source. This processing may be broken into the following steps, some of which are optional if the errors are not significant:

- Translate field image data formats to a format compatible with that used by the LIRL.
- Subtract electronic noise background from the data channel. Images that represent the electronic noise in the camera CCD (charge-coupled device) chip are acquired a few seconds before event zero time, then transmitted to the LIRL along with the data.
- Perform spatial corrections, if indicated. Such modifications are easy to perform if errors can be corrected by an overall change of scale, a set of shifts, or a rotation. If higher-order errors or oscillations occur, this step is difficult and time-consuming. Simple rotations and linear change-of-scale modifications are routinely done.
- In the case of EL-PINEX, a shading correction is usually needed. Because the radiation of interest is penetrating, a pinhole must be long, extending through several centimeters of dense material, to be effective. Therefore, any source point that is not on axis cannot be viewed clearly through the pinhole. The further off-axis a point is, the more obstructed the view becomes, and the dimmer the corresponding image point becomes. The shading correction enhances the brightness of the off-axis points to correct for this effect.
- Data are usually converted to physical units using the flat-field images recorded during the camera-calibration process. If the data are reasonably linear (as they are designed to be), then the appearance of the final imagery is not dramatically changed by this step.
- In the case of streak-camera data, the signal streaks are integrated over the width of the streak (that is, transverse to the streaking or sweeping direction), then extracted as a signal. Similarly, time is defined by relating the position along the data-streak to a sequence of pulses, called a “comb,” that have a known inter-pulse time interval.
- Just as with the EL-PINEX flat fields, streaks are recorded at several known constant excitation levels to provide a linearity curve for streaks. We then use these data along with the time information provided by the comb signal.
- Often, it is possible to generate images that display event predictions alongside the actual event data.

This list of processing corrections is formidable. Although some of the steps are nearly trivial, other steps are very complex and it takes much effort to perform them successfully. Many of these functions have been implemented in the IDL package mentioned above, because it is relatively easy to write complicated image-handling routines in that language. A good example is the routine that applies physical units to an image from the flat fields (see Figure 4). The concept and procedures that allow such a pixel-by-pixel calibration of images are also applicable to the signals extracted from streaks (see Figures 4 and 5). The IDL program that performs this calibration step is very short and simple. The routines that do the image calibration are nearly identical to those that do the signal calibration.

Yet another example of the ease with which an application may be developed with IDL is the routine that extracts a time base from the comb signal. This routine must find the peaks in the train of pulses, then perform an analysis to determine their position accurately. As this occurs, the routine makes a plot of the comb and inserts markings denoting the position found for each peak (Figure 6). An interpolation routine then finds the correct time for each sample of the signal on the basis of the time between pulses. A second plot is then made that displays the linearity of the time-vs-peak position, followed by a calculation that finds the camera sweep speed vs time. All of this is done in slightly more than a page of programming. This time base can then be applied to the calibrated data to display a final volts-versus-time signal, as shown in Figure 7.

Often, different EL-PINEX cameras view the same source in an experiment. Comparison of these images requires accurate registration of one image to the other. We have therefore developed a technique to allow visual registration of two images that are known to differ only by shifts and rotations. Above a threshold, one image is converted to a flat level 0.5, while the other image is set to flat level 1. When these images are summed, the resulting four-color display clearly shows where each image is located relative to the other, and where the images overlap (Figure 8). Interactive manipulation of shifts and rotations, along with fast redisplay of the four-color representation, allows a quick

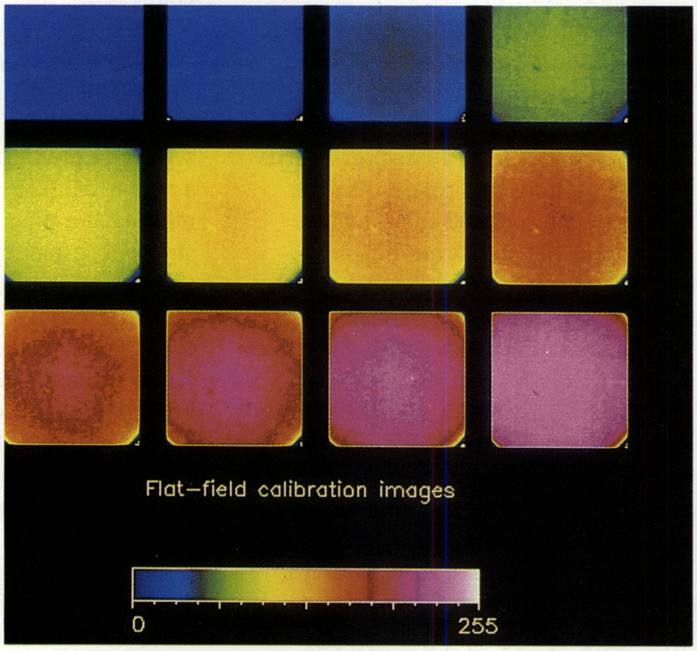

Figure 4. **These images show a progression in flat-field levels from low to high (blue to white). Each field is taken at a known intensity level and allows a pixel-by-pixel conversion of images to real physical units.**

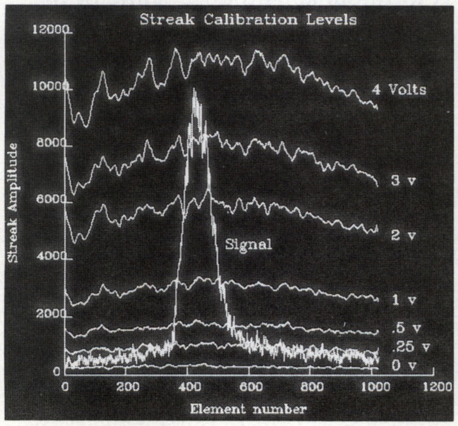

Figure 5. **The same concept as shown in Figure 4 applies to streak camera signals, where streaks taken at known intensity levels (as in Figure 2) allow point-by-point calibration to real physical units.**

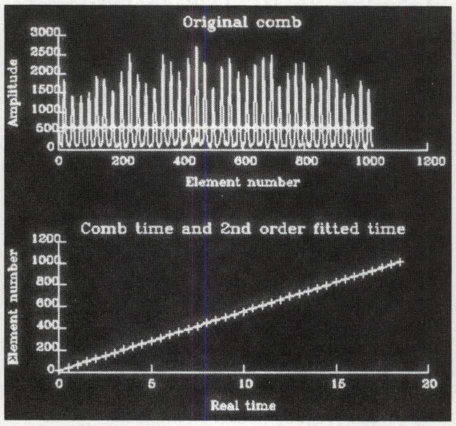

Figure 6. **The comb signal (from Figure 2) has been extracted from the streak image. The timing information is extracted using a routine written with the IDL interactive language, which can apply to both signals and images.**

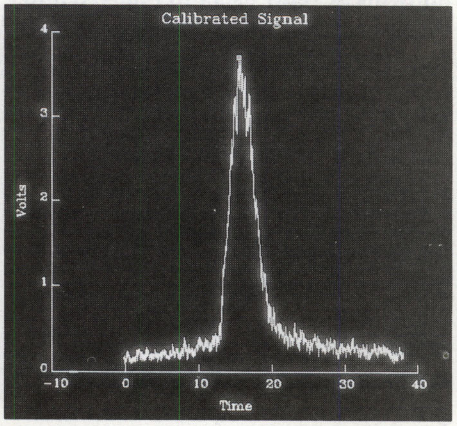

Figure 7. **The marker signal has been converted to volts vs time, using the calibration signals shown in Figure 5 and the timing information from the comb signal in Figure 6.**

alignment of images. This technique is analogous to moving one piece of transparent film over the other by hand.

Once the obvious problems have been corrected, the biggest challenge is to determine how to display the data effectively. Images can be shown in a multitude of ways, featuring various mathematical transformations, or

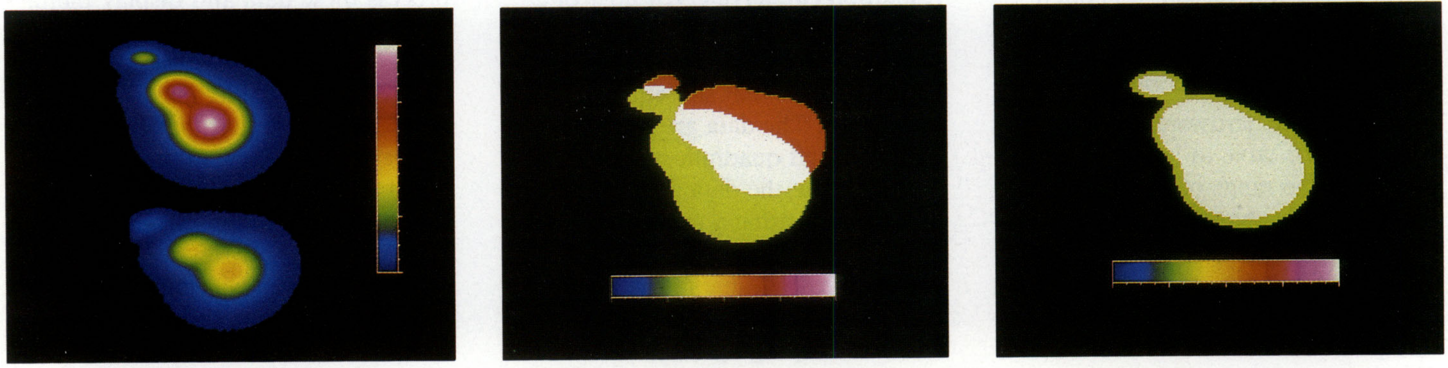

Figure 8. **Visual registration of images is simplified when each image can easily be seen separately and overlaps identified. Here, one image (three Gaussian pulses) is set to constant value 0.5 where pixel values are above a threshold; the other is set to 1.0. The sum is then displayed as a four-color image clearly showing their relative alignments. By interactively specifying shifts and rotation, the images can be quickly aligned.**

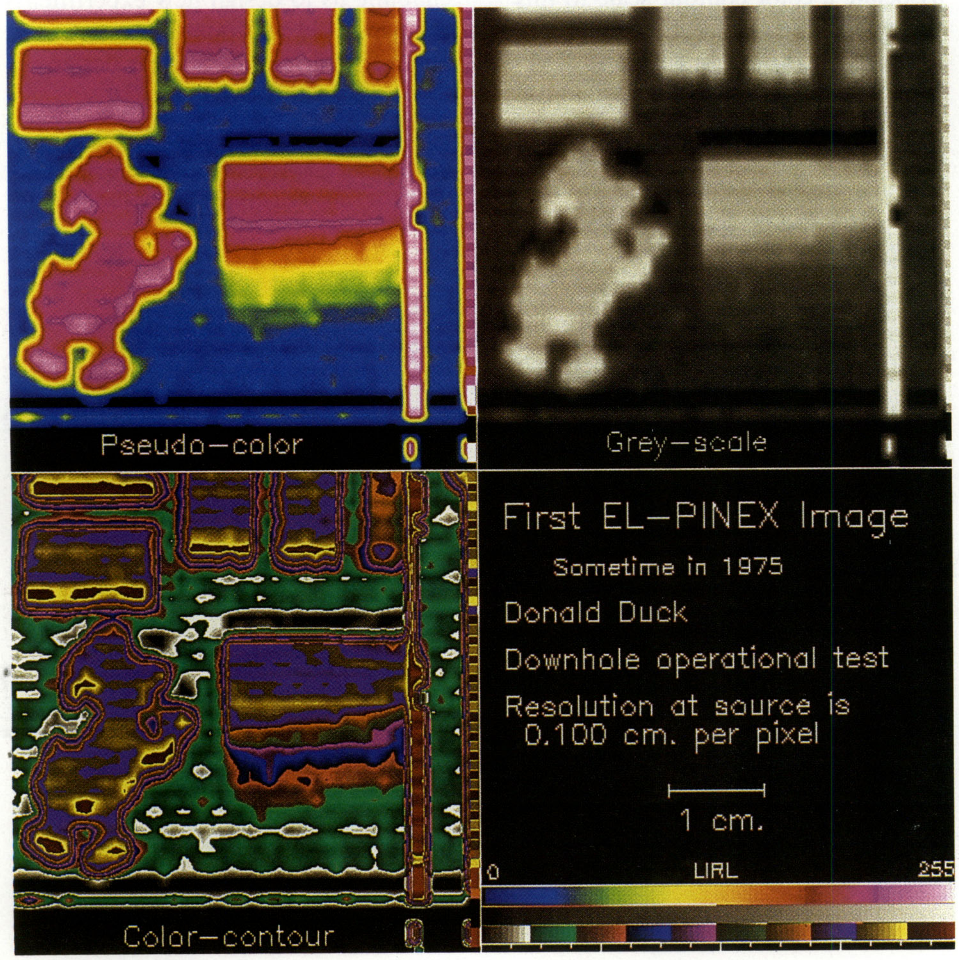

Figure 9. **The first electronic image sent uphole in the environment of a nuclear explosion, as a test of the concept and equipment. The image represents a mask which was recorded downhole at the time of an event. Close inspection of these images shows that each presentation emphasizes features that are not easily seen in the others.**

through the use of many specially designed color tables. Each display can emphasize certain features in the data, while other displays can hide or at least deemphasize those same features. For this reason, it is often desirable to see several different displays of the same image together at one time.

The display hardware allows only a single color table to be active at one time over the range of displayed data. If the data are shown with a color table that varies smoothly and slowly, the human eye may have difficulty distinguishing certain features since it requires contrast for effective visualization. We have used a presentation scheme to offer us several simultaneous views of the same data using visualization techniques that aid our interpretation of the data.

An example of this data presentation is shown in Figure 9. First, the original eight-bit data are divided by 3 so that values on the range 0 to 255 are compressed to the range 0 to 85 and the color table (blue to white) now corresponds to the numerical range 0 to 85 (each number in the new range now covers three numbers in the original). While we have decreased our numerical resolution (we have given up 1 or 2 bits), we have increased visibility and overcome the hardware limitation that would prevent subsequent operations. The data are shown in the upper left quadrant in Figure 9. Next we take the data and create a presentation using a gray scale. The method is straightforward in that we add 85 to each value in the previous presentation (we now span 85 to 170) and associate a gray scale with this range. This presentation is shown in the upper right quadrant in Figure 9. Finally, we again add 85 to change the span to cover 170 to 255 and associate a color contour scale to this range with the results shown in the lower left quadrant in Figure 9. The different attributes of each presentation scheme are evident to the experienced viewer, while in the hands of an experienced data interpreter the presentation is a powerful tool.

Conclusions

Over the years, the acquisition of image data, along with the ability to process these data and display them, has become increasingly important to the Nuclear Test Program. We now have easily available, inexpensive computer equipment that enables us to perform analyses on data that we could only dream about a few years ago. Using these new imaging tools, every portion of the cycle of camera preparation, data collection, and data processing is easier, faster, and more comprehensive. With these new capabilities, we can perform new experiments. This trend of increasing processing power promises to continue in the foreseeable future, enabling us to design new experiments to answer old and puzzling questions about the physics of nuclear designs.

Key Words: electronic pinhole experiment (ELPINEX); imaging systems; L-Division Image Research Laboratory (LIRL); Nevada Test Site; oscilloscopes; streak cameras.

Computational X-Ray Holography

We are using numerical simulations and visible-light experiments to explore the possibilities for an x-ray microscope for biological research.

For further information contact
Thomas J. Yorkey (415) 423-7504,
James M. Brase (415) 422-6992, or
Gregory A. Clark (415) 423-9759.

One of the first uses of the microscope was for the examination of living and dead tissue. Indeed, bacteria, whose existence was unsuspected, were first seen through a microscope. In the four centuries since its invention, we have made better and better light microscopes; still, the smallest objects that can be seen with them can be no smaller, approximately, than half the wavelength of the light.[1] Viruses and many structures of interest in living cells are much smaller than half the wavelength of visible light.

Viruses and intracellular structures can easily be seen with the electron microscope, which has a resolution one thousand times greater than the resolution of the light microscope (see the box on p. 38). However, one cannot examine a living cell with an electron microscope; the biological sample must be dehydrated, doped with heavy (metal) atoms, and placed in a vacuum. Thus there is always concern as to whether the sample so examined truly resembles the living specimen.

To examine living cells at a resolution greater than is possible with a light microscope, we must probe the specimen with shorter wavelengths. Since we want to look at intracellular structures, the optical properties of these structures and intracellular fluid must be sufficiently different at any wavelength that we select. For this and other reasons, we are considering wavelengths near 4 nm—soft x rays. Although these x-ray wavelengths are about a hundred times shorter than those of visible light, technical constraints may limit the resolution of a soft-x-ray microscope to only about ten times that of the light microscope—a significant accomplishment nonetheless.

Experiments aimed at building an x-ray microscope had to wait until the 1970s when the technologies of x-ray sources and x-ray optics were sufficiently developed. Technical developments since then indicate that by combining holographic techniques with an x-ray microscope, we may be able to examine individual living cells in three dimensions.

However, before we can develop an x-ray microscope, a number of problems or questions must still be resolved. First, we need coherent x rays of a suitable wavelength. The laboratory x-ray lasers being developed at LLNL have worked at wavelengths from 20.9 to 5.0 nm, which is almost short enough for our requirements regarding contrast between intracellular fluid and structures. Another problem has to do with cell damage; the cell will probably be damaged and disrupted by the absorbed x-ray energy, but we do not know whether we will have enough time before cell disruption to capture an image. A third problem concerns the small number of photons that would reflect or scatter off the object of interest and reach the detector. Advanced data-resolution techniques will be needed to extract information from such an "image."

In our preliminary investigations we have numerically simulated the performance that we can expect (ignoring the problems of cell damage and the small number of photons reaching the detector). The process of simulation has two computational steps. In the first step a (simulated) object scatters a propagated coherent plane wave. The new field is recorded, giving us a simulation of a real intensity distribution (a hologram) on a piece of film. In the second step a coherent plane wave propagates through the hologram, which scatters it. At a certain distance, the intensity distribution of the scattered plane wave approximates that of the field near the original simulated object.

Computed Holograms

An object (a cell, say) in an electromagnetic field (visible light, for example) distorts the field. We can use the distortion to infer the object's presence, details of its shape, and other characteristics. The object of interest is called the scattering object, and the illumination is the incident field.

If we make the assumptions that the incident field is harmonic in time and that the scattering object is isotropic (that is, its properties are independent of the direction of our measurement), then we can derive a homogeneous scalar Helmholtz equation. The solution of this equation will give the field everywhere. This implies that if we could record the field (amplitude and phase) in one place, we could calculate what it is in any other place—that is, we could (for example) make an "image" of an object of interest.

Resolution of Light, X-Ray, and Electron Microscopes

To illustrate the different resolutions of light, x-ray, and electron microscopes, first consider what you can see of the surface structure of the full moon on a clear night—merely variations in shading corresponding to *maria* and mountains. The effect of the finest light microscope is comparable to the improvement in being transported to a viewing point 100 m above the surface of the moon, where you could make out the shape of rocks with dimensions somewhat less than a meter. The effect of an electron microscope would be equivalent to being lowered to the moon's surface, where you could lie down and examine it from a height of about 10 cm. At that distance, not only could you comfortably read the boot manufacturer's emblem in a footprint, you could distinguish individual grains of lunar sand. The effect of an x-ray microscope would be intermediate between these two positions, or 10 meters above the surface. You could easily see the footprint, but you could not read the emblem.

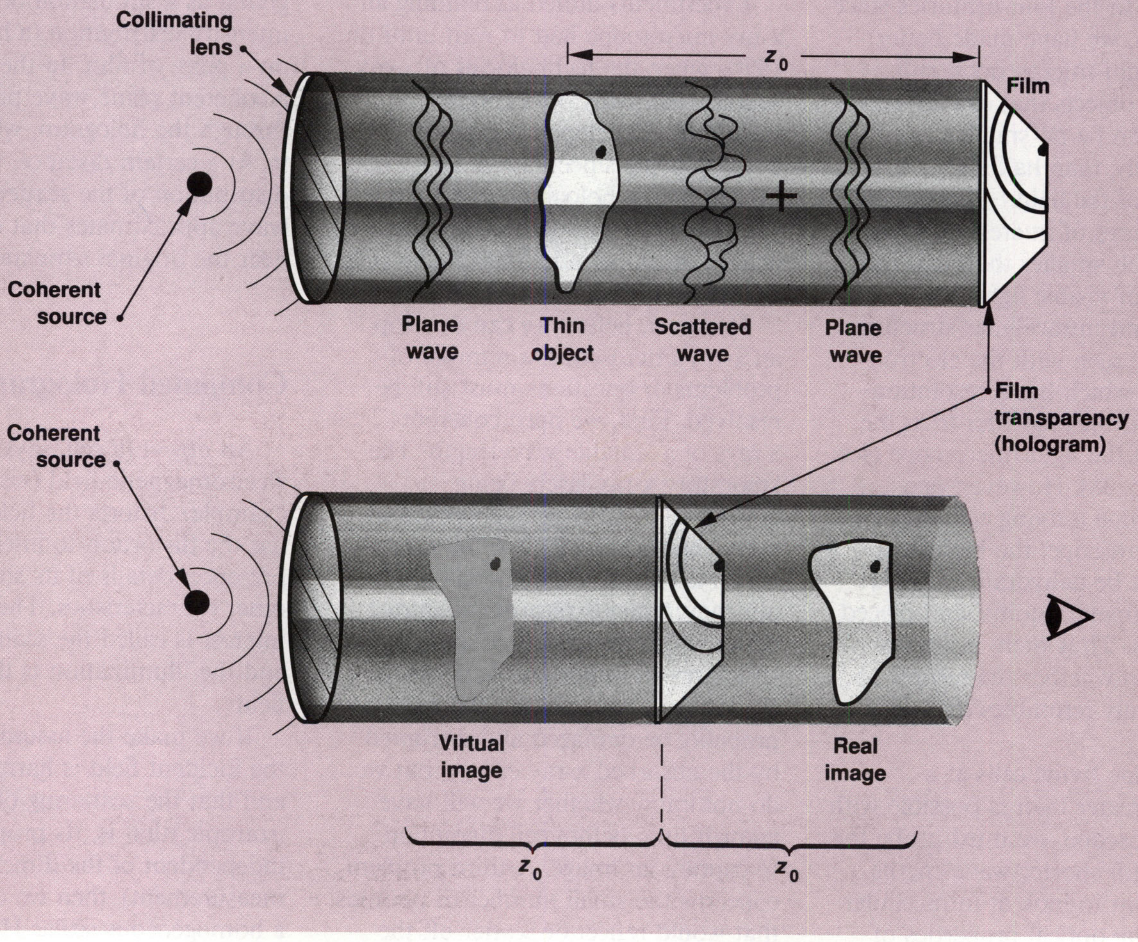

Solving a Helmholtz equation is very difficult except for special cases. We use two different methods based on different approximations. One method, based on the Fresnel integral, works well if the sample or object is thin. The other method, based on the Born approximation, is more suited for samples with appreciable thickness. We find by the second method that the cell resolution can be improved by taking several views from different angles.

To use the Fresnel integral, we assume that the incident field is a plane wave and the scattering object is thin, and then we determine the field on some specified plane. Using this approach, we have computed holograms for many objects. Figure 1 is an example of a computed hologram of a "rod." We can reconstruct the exact location and size of the rod from such a hologram.

Eliminating the Virtual Image

If we pass a plane wave of light through the film, the recording medium for the hologram (Figure 1b), two waveforms emerge from the other side of the film. A converging waveform comes to a focus exactly z_0 from the film. The resulting image is called the real image, which resembles the original object. The second waveform is diverging, which makes another image, called the virtual image. The apparent positions of the two in-focus images would be on opposite sides of the film hologram.

In Gabor holography, the real image cannot be viewed in focus without an accompanying out-of-focus virtual image, which of course interferes with viewing the real image. In our case, the reconstructed image itself does not represent the familiar visual image of the rod because of the presence of the diverging virtual image (see the box on Gabor holography on p. 43).

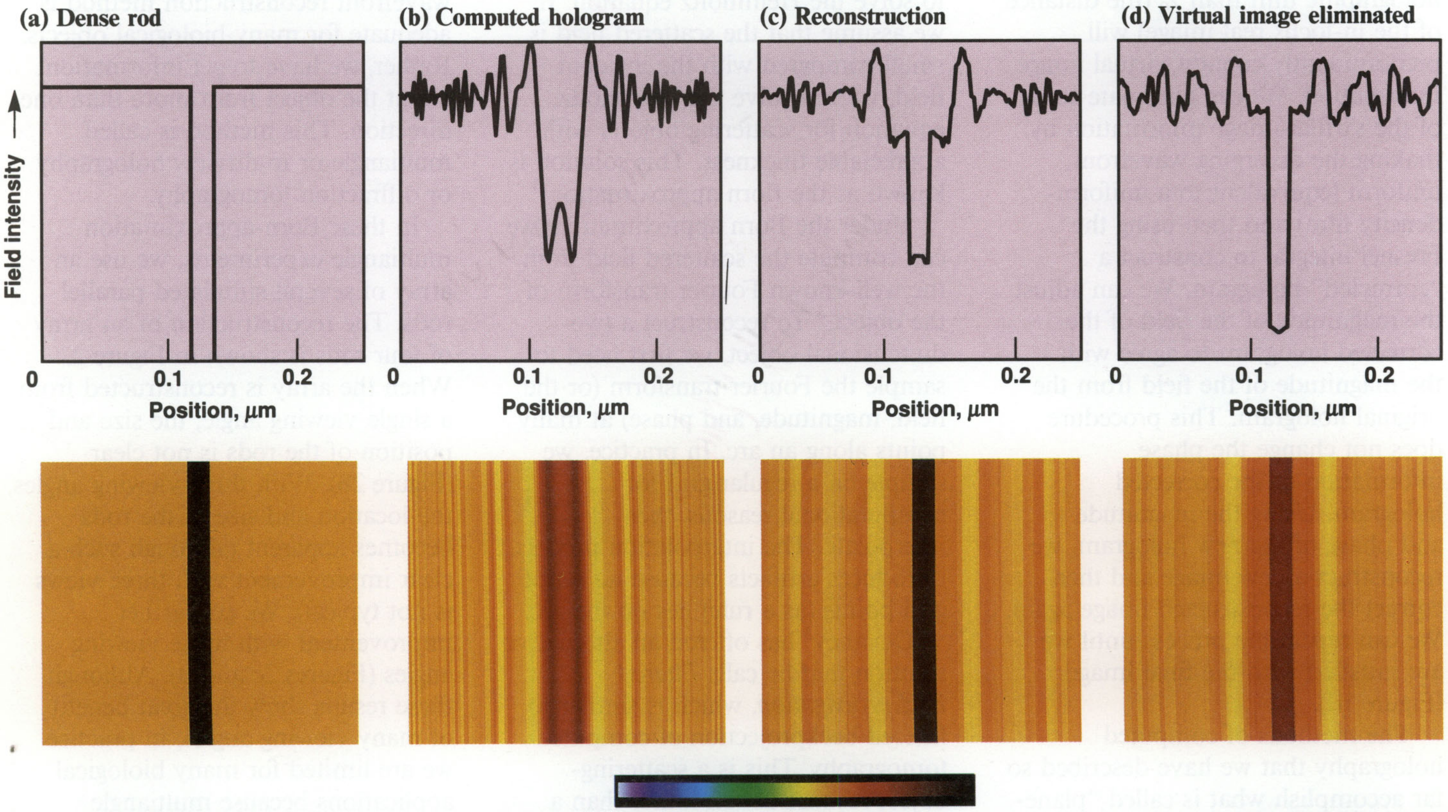

Figure 1. These panels show various forms of holographic recording and reconstruction of a simple form, namely a dense rod. The dense rod appears (computationally) as an opaque strip, shown in (a). A computed hologram is shown in (b). The color strip covers the same range as the field intensity ordinate. From the information in (b), we try to reconstruct the rod, i.e., its size and position. The result is shown in (c), which is clearly quite different from (a). That is because (c) also contains information about the virtual image, which interferes with the reconstructed real image. We eliminate the virtual-image information (d) with an iterated phase-retrieval algorithm.

There are many tried and untried techniques to eliminate the virtual image. Since it exists because the film can directly record only the magnitude of the field, not its phase, these techniques for removing a virtual image actually work by retrieving the phase of the recorded field. To retrieve the phase of the field, we need to incorporate additional information about the scattering object (for example, its size or shape). These techniques require that the reconstructed image and the hologram be digitized and recorded.

In one of these techniques,[2] we exploit the fact that the virtual image is diverging. Therefore, the peripheral wavefronts in a plane further from the holographic film than z_0 (the distance of the in-focus real image) will predominantly contain virtual image information. We can eliminate some of the virtual-image information by making the diverging wavefront uniform (equivalent to a uniform-density film) and then using the Fresnel integral to construct a "corrected" hologram. We can adjust the magnitude of the field of the corrected hologram to agree with the magnitude of the field from the original hologram. This procedure does not change the phase information of the corrected hologram. Using the magnitude and phase of the new hologram, we reconstruct a new image and then correct the reconstructed image again. We can repeat the process until we are satisfied with the final image (Figure 1d).

The methods of computed holography that we have described so far accomplish what is called "plane-to-plane reconstruction"; from information recorded in one plane, we can infer the (scattering) nature of an object in another plane. However, the object must be very thin, so this method has limited promise for examining tissue or individual cells. We regard these reconstructions as preliminary experiments that have given us valuable insights and from which we have gained experience with experimental procedures, optical setups, and computational routines.

Imaging Objects of Significant Thickness

To image objects of biological interest (with depth or thickness of more than a few nanometers), we must apply a different approximation to solve the Helmholtz equation. If we assume that the scattered field is small compared with the incident field, we can solve the Helmholtz equation for scattering objects with appreciable thickness. This solution is known as the Born approximation.[3]

Under the Born approximation, we can compute the scattered field from the well-known Fourier transform of the object.[4] To reconstruct a two-dimensional object, we first need to sample the Fourier transform (or the field, magnitude, and phase) at many points along an arc. In practice, we sample on a regular grid for computational reasons, then interpolate. The interpolation process introduces artifacts because no set of grid points (as a rule) lies on the arc.

Devaney[5] has offered an alternative solution that he calls *filtered backpropagation*, which is similar to filtered backprojection of computed tomography. This is a scattering-object reconstruction rather than a field-intensity method. The method introduces filters (which may be two- or three-dimensional) in propagating back an estimate of the object from the hologram to the real object. The filter is applied to the original hologram, and then the scattering object is computed. The filters extract "properties" of the scattering object's z-axis (depth) from the hologram.

A three-dimensional object cannot be completely represented by information coming to a small plane. For example, it is impossible to distinguish between the images of a basketball and the "front" half of the basketball viewed from the same position. One needs more than one point of view (or an infinite plane) to obtain information about the "hidden" surface(s) of the object. Therefore, no practical plane-to-plane wavefront reconstruction method is adequate for many biological objects. Rather, we have to get information about the object from more than one direction. This method is called multiangle or multiview holography or diffraction tomography.

In these Born-approximation multiangle experiments, we use an array of several simulated parallel rods. The reconstruction of an array of four rods is shown in Figure 2. When the array is reconstructed from a single viewing angle, the size and position of the rods is not clear (Figure 2b). With three viewing angles, the location and size of the rods becomes apparent (although such a clear improvement with three views is not typical). We get further improvement with more viewing angles (Figures 2c and d). Although these results show the great benefit of many viewing angles, in practice we are limited for many biological applications because multiangle recordings of a changing object must be simultaneous.

Optical Experiments

To verify some of our computational results, we have begun experiments with visible light (single-view holography). We have recorded holographic images on film and with a digital camera, then transferred the digital information to a computer. Thereafter, all transformations of the information are computationally performed—we do not use any light imaging for reconstruction.

The simplest example again is the rod or opaque strip. To produce this strip, we use a fine wire, 26 μm in diameter, or about one fifth the diameter of a human hair (Figure 3a). Figure 3b shows a hologram of the wire and Figure 3c shows the reconstruction of the wire by the Fresnel integral; the reconstruction still contains the unwanted virtual image. We remove the virtual image by the phase-retrieval algorithm; Figure 3d shows the result of 10 such iterations.

A more complex example is shown in Figure 4. Here, we used a collection of a few 5-μm-diameter polystyrene spheres. The collection was about 25 μm in diameter. We reconstructed images from optical holograms made with a green laser. The result in Figure 4c shows that structure down to about 5 μm can be resolved.

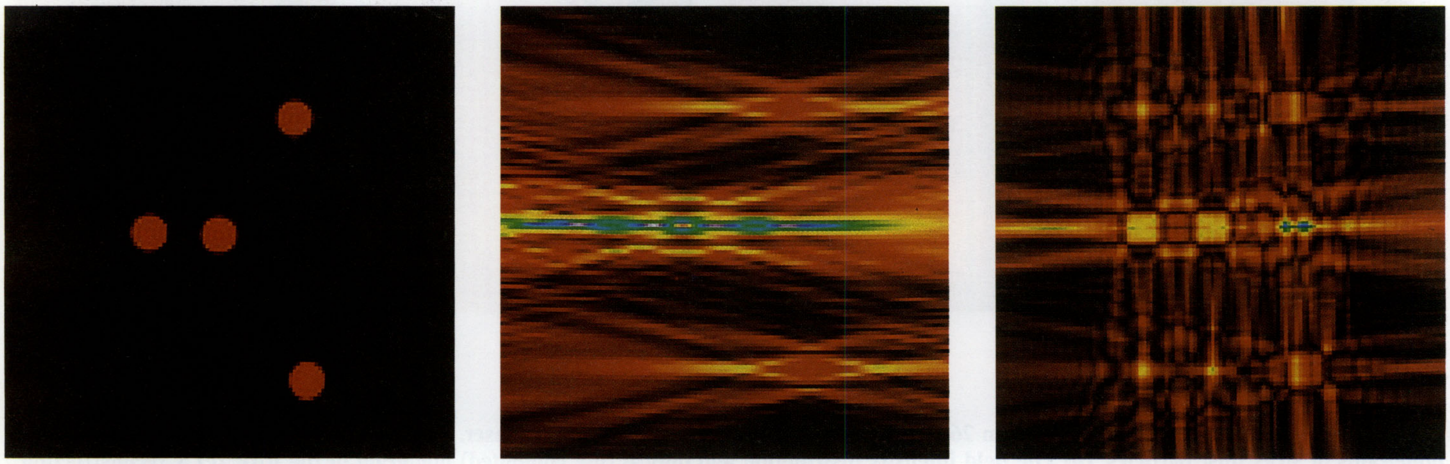

(a) Simulated array

(b) Single-view reconstruction

(c) Two-view reconstruction

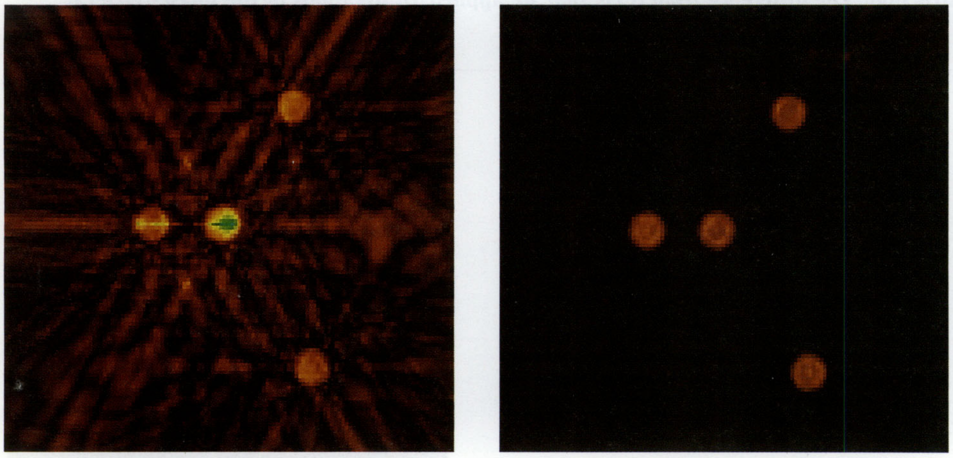

(d) Three-view reconstruction

(e) Twenty-view reconstruction

Figure 2. This example demonstrates multiview holography within the Born approximation, showing the effect of increasing the number of views. (a) The scattering object is an array of four rods. (b) The reconstruction of the array from the data of a single viewing angle. (c), (d), and (e) The reconstruction is improved by using the data from more viewing angles.

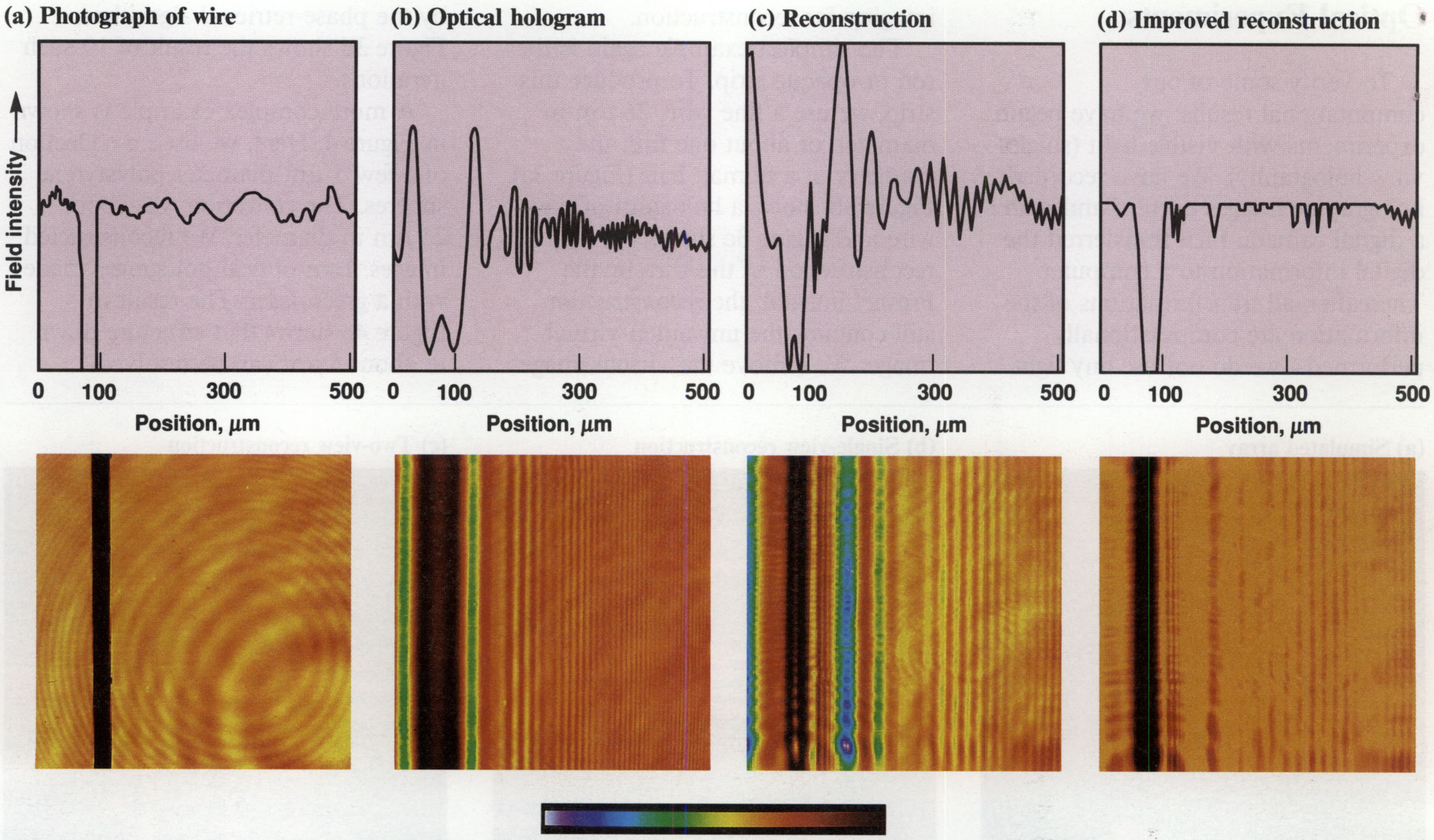
(a) Photograph of wire (b) Optical hologram (c) Reconstruction (d) Improved reconstruction

Figure 3. (a) The in-focus photograph of an 26-μm-diam wire illuminated with a 0.5-μm laser. The two sets of concentric circles are holograms of stray dust particles. (b) The field intensity distribution and optical (not computed) hologram of the wire. (c) A reconstruction of the field intensity distribution and hologram of the wire using a Fresnel integral. This reconstruction contains unwanted information about the virtual image. (d) An improved reconstruction. The difference from (c) is that we applied 10 iterations of the phase-retrieval algorithm.

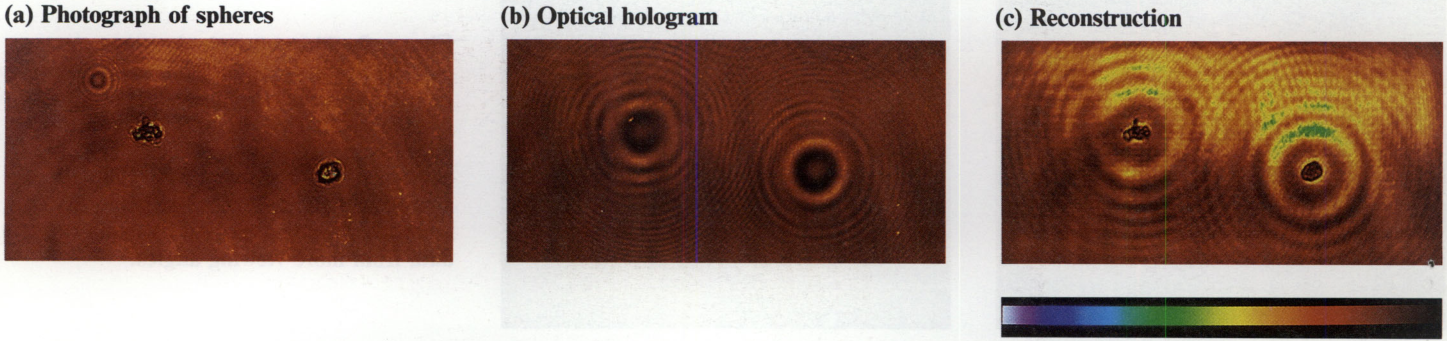
(a) Photograph of spheres (b) Optical hologram (c) Reconstruction

Figure 4. The in-focus image (a), the hologram (b), and the Fresnel reconstruction (c) of a few 5-μm polystyrene spheres.

Gabor Holography

One of the simplest arrangements for creating a holographic image was invented by Denis Gabor and is described in many introductory optics texts.* It is simple in that it calls for a minimal number of optical components.

The object of interest, which must have a high average transmittance, is illuminated by collimated coherent light, the incident wave. Where the wave passes through the object, the light is attenuated and deflected or scattered. Consequently, the light arriving at any point beyond the object comes partly from the attenuated incident wave and partly from light forward-scattered by other parts of the scattering object. The scattered light arrives with a slight delay, because it has traveled farther. The delay then represents phase information. The forward-scattered wave and the directly transmitted portion of the incident wave interfere, and the interference pattern is recorded as intensity variations in a photographic film at a convenient distance from the object. Thus the recorded intensity pattern depends on both the amplitude and the phase of the scattered wave (with respect to the incident wave).

The developed film represents the hologram—it contains amplitude and phase information about the scattered wave, and thus about the object. A hologram is different from a simple shadow, which contains no information that depends on the wave nature of the illumination. An image of the object can be reconstructed from the hologram by numerical methods or by illuminating a transparency of the hologram with coherent light (normally of the same wavelength as in the original recording). When the hologram is illuminated with collimated light, two images are formed, referred to as the real and virtual images. Visually, the two images interfere with each other, so variations of optical arrangement have been devised to separate the images.

---

* This account draws on J. W. Goodman, *Introduction to Fourier Optics* (McGraw-Hill, San Francisco, 1968). Gabor reported his original work in "A New Microscope Principle," *Nature*, **161**, 777 (1948).

Future Work

X-ray microscopy in general and our project in particular are developing rapidly. We are planning further experiments to enhance the reconstruction of depth information. Our Born-approximation method can be verified by reconstructing real objects. Another method that looks very promising is the use of spherical incident waves instead of plane waves. A spherical wave from a close source could be used to make the equivalent of holograms from many viewing angles simultaneously. One of our next endeavors will be to introduce real and simulated objects that are more similar in refractive properties to biological objects of interest, in preparation for the advent of lasers at suitable x-ray wavelengths.

Key Words: Born approximation; diffraction tomography; filtered backpropagation; Helmholtz equation; holography—computed, Gabor, multiview; microscope—x-ray; plane-to-plane reconstruction.

Notes and References

1. To give some idea of the size of the wavelength of light: it would take green light about 1000 wavelengths to cross the period at the end of this sentence.
2. G. Liu and P. D. Scott, "Phase Retrieval and Twin-Image Elimination for In-Line Fresnel Holograms," *J. Opt. Soc. Amer., A* **4**, 159–165 (1987).
3. S. X. Pan and A. C. Kak, "A Computational Study of Reconstruction Algorithms for Diffraction Tomography: Interpolation versus Filtered Backprojection," *IEEE Trans. Speech, Signal Processing* **31**, 1262–1275 (1983).
4. The Fourier transform of an object is the expression of its character (usually its shape or its scattering properties in this context) in terms of the sinusoidal frequency components with which it can be represented. Some problems become simpler to solve with the use of Fourier transforms. A good introduction to Fourier optics is J. W. Goodman, *Introduction to Fourier Optics* (McGraw-Hill, San Francisco, 1968).
5. Anthony J. Devaney, " A Filtered Backprojection Algorithm for Diffraction Images," *Ultrasonic Imaging* **4**, 336–350 (1982).

Abstracts

Neutron Penumbral Imaging of Laser-Fusion Targets

Neutron penumbral coded-aperture imaging has been used to obtain the first neutron images of laser-driven inertial confinement fusion targets at the Nova laser facility. The images provide a direct measurement of the deuterium-tritium burn region within a compressed target. The performance of this new imaging system is in good agreement with predictions based on both numerical and theoretical models. System resolution and sensitivity are being improved through changes in the aperture and detector. We anticipate that future improvements will enable us to achieve a two-point resolution better than 10 μm with enough sensitivity to allow the imaging of radiation-driven targets that reach a high radial convergence and produce yields of 10^{11} neutrons or less. Such an enhanced imaging system will be a valuable asset for future inertial confinement fusion research.

Contact: Richard A. Lerche (415) 422-5364 or David B. Ress (415) 423-8195.

Computed Tomography for Nondestructive Evaluation

Computed tomography (CT) has been used for nearly 20 years for medical purposes but not for nondestructive evaluation of industrial materials and assemblies. We explore the differences between these two modes of operation and describe the status of current and planned research in the use of CT technologies for industrial inspections at LLNL. Our efforts are divided among building of different types of CT systems, reconstruction techniques, and analysis and display methods.

Contact: S. G. Azevedo (415) 422-8538, H. E. Martz (415) 423-4269, or J. M. Brase (415) 422-6992.

Three-Dimensional Image Analysis for Studying Nuclear Chromatin Structure

We have developed an optical/electronic system for capturing cross-sectional views of cell nuclei in digital form and transferring them to a computer for image analysis. The computer combines information from many of these two-dimensional images to reconstruct the three-dimensional structures they represent. We plan to use this equipment to study the arrangement of chromosomes in intact cell nuclei, using fluorescent hybridization to tag individual chromosomes for better visualization. Our goal is to determine what the normal arrangement of chromosomes may be, and the extent to which deviations from the norm can affect cell function or even correlate with clinical diseases or syndromes.

Contact: Phillip N. Dean (415) 422-6293.

Imaging in the Nuclear Test Program

The acquisition, processing, and display of data in the form of images has become increasingly important to the Nuclear Test Program. Using inexpensive new computer imaging tools, we now are able to perform every portion of the cycle of camera preparation, data collection, and data processing more easily, speedily, and comprehensively than before. With these new capabilities, we can perform new experiments. This increase in processing power promises to be a continuing trend that will enable us to design new experiments to answer old and puzzling questions about the physics of nuclear designs.

Contact: Eric Frerking (415) 422-6942.

Computational X-Ray Holography

Visible-light experiments and numerically simulated holograms are being used to test ideas about the performance of an x-ray microscope suitable for biological research. For simple Gabor holography, the plane-to-plane reconstruction via the Fresnel integral contains unwanted virtual-image information. We computationally reduce or eliminate the virtual image by taking advantage of other knowledge about the object of interest. To obtain information about depth, we use the Born approximation, which assumes a small amount of scattering, and filtered backpropagation for the reconstruction. Our studies show poor longitudinal resolution with a single view and great improvement with multiview holography. These investigations begin to define expectations for the performance of an x-ray microscope suitable to examine objects of the size of cells and cell structures of living specimens.

Contact: Thomas J. Yorkey (415) 423-7504, James M. Brase (415) 422-6992, or Gregory A. Clark (415) 423-9759.

Recent Titles

Articles published in recent issues of* Energy and Technology Review *are grouped below according to their chief sponsors. Generally, these are the Assistant Secretaries of the U.S. Department of Energy. Research funded by other federal agencies is listed under Work for Others. Research funded by the Laboratory and general overviews are grouped under LLNL.

DEFENSE PROGRAMS

Inertial Fusion

Neutron Penumbral Imaging of Laser-Fusion Targets (October 1988)
Gas Cooling of Laser Disks (May 1988)

Military Application

Computed Tomography for Nondestructive Evaluation (October 1988)
Imaging in the Nuclear Test Program (October 1988)
Modeling Plasticity in a Two-Phase Ductile Material (September 1988)
Measuring the Performance of Supercomputers (May 1988)
Composite Materials: Characterizing Their Mechanical Properties (April 1988)
Discovery of Two New Long-Lived Isotopes: ^{261}Lr and ^{262}Lr (March 1988)
Search for ^{272}[109] in a New Region of Stability (March 1988)
The Lightning-Invulnerable Device System (March 1988)
Detonation of Explosives in Accidents (January·February 1988)
The Detonation of High Explosives (January·February 1988)
Formulating High-Explosive Materials (January·February 1988)
High-Explosive Diagnostics (January·February 1988)
Synthesis of Energetic Materials (January·February 1988)

ENERGY RESEARCH

Understanding Particulate Flow Behavior (September 1988)
Microwave Tokamak Experiment (May 1988)
Development of an Aluminum-Air Battery for an Electric Vehicle (April 1988)
The Rotating Target Neutron Source (March 1988)

LLNL

Institutional Research and Development

Computational X-Ray Holography (October 1988)
Recombinant DNA Biotechnology and the Bioconversion of Metals (April 1988)

Overviews

Numerical Methods for Solving Ordinary Differential Equations and Differential/Algebraic Equations (September 1988)
The State of the Laboratory (July·August 1988)

WORK FOR OTHERS

Computer-Aided Information Science and the Intelligent Gateway Processor (June 1988)

Defense Advanced Research Projects Agency

Gas Cooling of Laser Disks (May 1988)

National Institutes of Health

Three-Dimensional Image Analysis for Studying Nuclear Chromatin Structure (October 1988)

Nuclear Regulatory Commission

Shipping Cask Analysis System (June 1988)
Transporting Spent Reactor Fuel Safely (June 1988)

U.S. Government Printing Office: 1988/10 – 585-057/8141

Technical Information Department · Lawrence Livermore National Laboratory · University of California · Livermore, California 94551

L- 53 (3)
Vault Reference
Bldg 127, Room 1093